Monthly Notices
of the
ROYAL ASTRONOMICAL SOCIETY

Mon. Not. R. Astron. Soc. **424,** 1346–1362 (2012) doi:10.1111/j.1365-2966.2012.21320.x

The jet–cloud interacting radio galaxy PKS B2152−699 – I. Structures revealed in new deep radio and X-ray observations

D. M. Worrall,[1⋆] M. Birkinshaw,[1] A. J. Young,[1] K. Momtahan,[1] R. A. E. Fosbury,[2] R. Morganti,[3,4] C. N. Tadhunter[5] and G. Verdoes Kleijn[4]

[1]*HH Wills Physics Laboratory, University of Bristol, Tyndall Avenue, Bristol BS8 1TL*
[2]*European Southern Observatory, D-85748 Garching bei München, Germany*
[3]*Netherlands Institute for Radio Astronomy, PO Box 2, 7990 AA Dwingeloo, the Netherlands*
[4]*Kapteyn Astronomical Institute, University of Groningen, Postbus 800, 9700 AV Groningen, the Netherlands*
[5]*Department of Physics and Astronomy, University of Sheffield, Sheffield S3 7RH*

Accepted 2012 May 15. Received 2012 May 14; in original form 2012 February 28

ABSTRACT

PKS B2152−699, which has radio power characteristic of sources that dominate radio feedback, is exceptional in showing a wide range of features associated with radio-galaxy/gas interactions. We present new deep radio (Australia Telescope Compact Array), X-ray (*Chandra*) and ground-based optical observations, and test the energetics of the feedback model. We report the first high-resolution observations of the radio jet, finding that the inner jet extends ∼8.5 kpc (10° viewing angle) in the direction of an optical emission-line high-ionization cloud (HIC) before taking a zigzag path to a position offset from the HIC. Jet synchrotron radiation to X-ray energies is seen. The HIC is associated with cool, $kT \sim 0.3$ keV, X-ray gas of anomalously low metallicity. On larger scales, the radio galaxy displays all three X-ray features that together confirm supersonic expansion of the lobes into the external medium: gas cavities, inverse Compton emission showing excess internal lobe pressure, and high-contrast arms of temperature above the $kT \sim 1$ keV ambient medium. The well-formed southern lobe on the counterjet side is expanding with a Mach number between 2.2 and 3. The lobe energy appears to be more gently dissipated in the north. We estimate a cavity power $\sim 3 \times 10^{43}$ erg s^{-1}, which falls well below previously reported correlations with radio power. The total inferred time-averaged jet power, $\sim 4 \times 10^{44}$ erg s^{-1}, is dominated by the kinetic and thermal energy of shocked gas, and if used instead would bring the source into better agreement with the correlations. The southern hotspot is the more complex, with a spiral polarization structure. Its bright peak emits synchrotron X-rays. The fainter northern hotspot is particularly interesting, with X-rays offset in the direction of the incoming jet by ∼1 arcsec relative to the radio peak. Here modest ($\delta \sim 6$) relativistic beaming and a steep radio spectrum cause the jet to be X-ray bright through inverse Compton scattering before it decelerates. With such beaming, a modest proton content or small departure from minimum energy in the jet will align estimates of the instantaneous and time-averaged jet power. The hotspots suggest acceleration of electrons to a maximum energy $\sim 10^{13}$ eV in the jet termination shocks.

Key words: galaxies: active – galaxies: individual: PKS B2152−699 – galaxies: jets – radio continuum: galaxies – X-rays: galaxies.

1 INTRODUCTION

The source PKS B2152−699 (hereafter 2152−699) is one of the brightest nearby (luminosity distance 123 Mpc, see below) radio galaxies in the southern sky (Schilizzi & McAdam 1975). It has attracted attention due to the presence of a high-ionization cloud (HIC; Tadhunter et al. 1987, 1988; di Serego Alighieri et al. 1988) that lies adjacent to a radio-bright knot near the base of the northern lobe (Fosbury et al. 1998), providing evidence for a strong jet–cloud interaction. Moreover, X-ray measurements with *Chandra* have discovered a large-scale X-ray-emitting atmosphere

⋆E-mail: D.Worrall@Bristol.ac.uk

containing cavities, interpreted as having been inflated by the lobes of the radio source (Young et al. 2005). 2152−699 is therefore an example of a radio source where feedback between the active galactic nucleus (AGN) and surrounding plasma can be well studied.

However, rather than just an example, 2152−699 has particular importance in the study of radio-source feedback since it is a nearby example at the characteristic radio power of sources that must dominate such feedback in the Universe as a whole (Worrall 2009). The total radio flux density is 68 Jy at 468 MHz, and $\alpha_r \sim 0.8$ ($S_\nu \propto \nu^{-\alpha_r}$; Kühr et al. 1981), giving a power extrapolated to 178 MHz of 2×10^{25} W Hz^{-1} sr^{-1}, and placing it in the range where FRIs and FRIIs overlap in luminosity (Fanaroff & Riley 1974). Its hotspots are embedded in its N and S lobes rather than at the extremities (Fosbury et al. 1998), which is a common morphology for sources close to the FRI/FRII border (Capetti, Fanti & Parma 1995). The luminosity function of radio sources places those at the FRI/FRII boundary as the population that contributes the greatest fraction of the overall radio output of active galaxies (Ledlow & Owen 1996; Kaiser & Best 2007). In combination with correlations between radio power and cavity power (Cavagnolo et al. 2010), it is therefore apparent that sources at the FRI/FRII boundary are those of most interest for studies of radio-mode feedback. A typical such source is not in a cluster atmosphere, unlike those to have received most attention to date (e.g. Forman et al. 2007; Fabian et al. 2011; Gitti et al. 2011). Characteristically, there is nothing extraordinary about the environment of 2152−699, increasing its importance as an exemplar of radio-source feedback.

Aside from the large-scale properties of 2152−699, study of the jet and hotspots has been limited to date by a lack of sensitive high-resolution radio mapping extending from the core to hotspots, rectified in this paper. Earlier papers have demonstrated that the jet must undergo deflection in order to terminate in the N hotspot. However, where that deflection occurs has remained uncertain. The very long baseline interferometry (VLBI) measurements of Tingay et al. (1996) found a pc-scale nuclear radio jet at position angle $44^\circ \pm 4^\circ$ from the core, whereas the N hotspot is at an angle of about 24° from the core. This led the authors to suggest that the jet is deflected by about 20° due to oblique shocks within the HIC, which also lies at a position angle of about 44° from the core. The situation became more complicated with the detection of radio emission from a knot lying close to the HIC but sufficiently separated to be at a position angle of about 34° from the core (Fosbury et al. 1998). The 18-GHz radio map presented in this paper reveals where the jet bends, and in conjunction with multiwavelength data we find some clues as to why.

Section 2 describes our new Australia Telescope Compact Array (ATCA), *Chandra* and ground-based optical observations, and our new processing of *Hubble Space Telescope* (*HST*) data. Measurements from these data are presented in Section 3, and in Section 4 we describe separately our deductions concerning the northern radio jet, the two hotspots, the HIC, and feedback as inferred from the properties of the radio lobes and hot-gas environment. Conclusions are summarized in Section 5. We adopt $H_0 = 70\,\mathrm{km\,s^{-1}\,Mpc^{-1}}$, $\Omega_{m_0} = 0.3$, $\Omega_{\Lambda_0} = 0.7$. 1 arcsec corresponds to 566 pc at the redshift ($z = 0.0282$) of 2152−699, and the luminosity distance is $D_L = 123$ Mpc. Spectral index, α, is defined in the sense that flux density is proportional to $\nu^{-\alpha}$: the photon spectral index measured in X-ray observations is $1 + \alpha$, and the energy index of the number spectrum of synchrotron-radiating electrons is $2\alpha + 1$.

2 OBSERVATIONS AND ANALYSIS METHODS

2.1 ATCA radio

We made a full-track observation of 2152−699 with the ATCA in its 6A array configuration with the Compact Array Broad-band Backend (CABB) correlator (Wilson et al. 2011) on 2009 June 22 (programme C2034). The observations were in two frequency bands centred at 17.0 and 19.0 GHz, each of bandwidth 2048 MHz divided into 2048 channels. The sources B1921−293 and B1934−638 were observed for bandpass and primary flux calibration, respectively. B2353−686, adjacent to 2152−699, was observed for phase calibration and as a pointing reference. Data reduction was carried out with the MIRIAD[1] software using the calibration advice for CABB data given in the 2010 September version of the MIRIAD User Guide.

Large time-dependent phase slopes were seen across the frequency bands, presumably due to atmospheric delays. To help correct for this, each band was divided into eight separate subbands in frequency for individual self-calibration and multifrequency synthesis cleaning, and results were combined for final mapping. The final map (Fig. 1) was made with uniform weighting and a 0.35 arcsec restoring beam. Noise in the map was dominated by residual phase errors. Nevertheless, except very close to the bright core, the dynamic range near the jet is 24 000:1, which is a notable achievement for a complex source at such a high frequency with a single ATCA east–west array configuration. It is of historical interest that 2152−699 was the first source to be imaged with the ATCA during construction in 1989, at 5 GHz with a 30 arcsec full width at half-maximum (FWHM) beam (Norris et al. 1990).

We make use of a map with a 2.35 arcsec restoring beam made from pre-CABB ATCA 4.74 GHz data taken in 1992 and presented in Fosbury et al. (1998). We applied an astrometric correction of 1.06 arcsec, mainly in declination, to align the core as seen on that map with that in our 18-GHz map.

2.2 *Chandra* X-ray

We made a 125 ks observation of 2152−699 in full window and FAINT data mode with the Advanced CCD Imaging Spectrometer (ACIS) on board *Chandra* in 2010. The observation was divided into exposures on January 20 (ObsId 12088) and January 22/23 (ObsId 11530). The source was positioned at the normal aimpoint of the front-illuminated I3 chip. The other three CCDs of ACIS-I and the S2 and S3 chips of ACIS-S were also on during the observations, giving a frame time of 3.24 s. Details of the instrument and its modes of operation can be found in the *Chandra* Proposers' Observatory Guide.[2] Results presented here use CIAO v4.3 and the CALDB v4.4.5 calibration data base. We re-calibrated the data to take advantage of the subpixel event reposition routine (EDSER), following the software 'threads' from the *Chandra* X-ray Center (CXC),[3] to make new level 2 events files. Only events with grades 0, 2, 3, 4, 6 were retained. After a small loss of exposure time due to eliminating periods where the background rate was more than 3σ from the average, the calibrated data sets have durations of 58.359 (ObsId 12088) and 56.352 ks (ObsId 11530).

A shorter earlier observation in full window and VFAINT data mode had been made with *Chandra* on 2001 August 2, as described

[1] http://www.atnf.csiro.au/computing/software/miriad
[2] http://cxc.harvard.edu/proposer
[3] http://cxc.harvard.edu/ciao

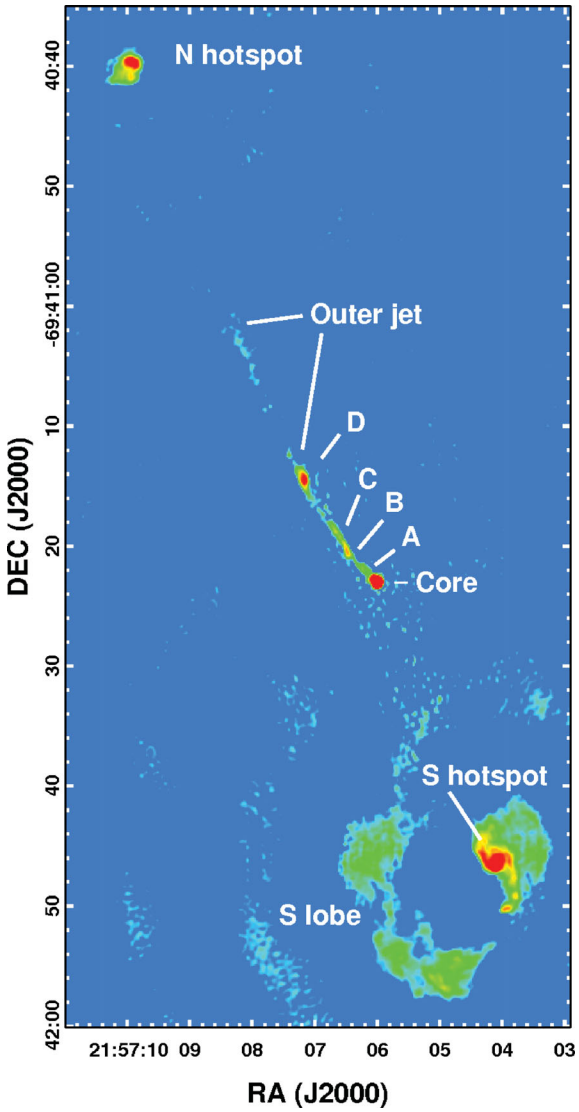

Figure 1. 18 GHz ATCA radio map with 0.35 arcsec restoring beam and source features labelled. The faint features to the east of the S lobe are residual grating rings from the bright S hotspot.

by Ly, De Young & Bechtold (2005) and Young et al. (2005). For that observation 2152−699 was positioned at the normal aimpoint of the back-illuminated S3 chip, and the S1, S2, S4, I2 and I3 chips were also on. We re-calibrated those data, as above, and applied VFAINT cleaning to help remove particle background. That data set has a final exposure time of time of 12.192 ks (ObsId 1627).

The astrometry of the X-ray images was adjusted to align with the 18-GHz radio core. Shifts were roughly 0.75 arcsec, mainly in declination. Our analysis uses combined data from the three observations. For display purposes we have made a merged exposure-corrected file. For spectral analysis we have fitted the same model parameters jointly to the individual data sets, using their respective calibration files.

For spectral fitting we have used XSPEC.[4] Where features are too weak to allow sufficient spectral bins containing at least 20 counts we have estimated parameter confidence ranges using the XSPEC-implemented CSTAT statistic applied to on-source and background regions separately. We used the APEC model for thermal components. All fits include absorption along the line of sight in our Galaxy assuming a column density of $N_{\rm H} = 2.52 \times 10^{20}$ cm^{-2} (from the COLDEN program provided by the CXC, using data of Dickey & Lockman 1990). Quoted errors are 1σ taking into account the number of interesting parameters.

[4] http://heasarc.nasa.gov/xanadu/xspec

2.3 WFI optical

We observed 2152−699 with the 2.2-m MPG/ESO 34-arcmin-field-of-view Wide Field Imager (WFI) using a *V*-band filter (number 843) for 3 ks in 2004 October. While the primary objective was to search for [O III]-emitting clouds aligned with the radio axes but further from the nucleus than the HIC, we use the data here to report optical emission from 2152−699's N and S hotspots, which lie beyond the field of view of the *HST* observation (Section 2.4). The data were reduced with two independent software packages, ALAMBIC (Vandame 2004) and ASTRO-WISE (McFarland et al. 2011), with fluxes agreeing to within ∼10 per cent and astrometry to ∼0.1 arcsec. The photometric calibration yielded a systematic error in the zero-point of ∼0.1 mag when calibrated to Johnson *V*. This budget includes errors in the extinction and colour terms of the standard stars, and varying illumination over the WFI chips. Johnson *V* magnitude was converted to flux density at 5.5×10^{14} Hz using 3.75×10^{-9} erg s^{-1} cm^{-2} Å^{-1} for 0 mag. We applied an astrometric correction of 0.5 arcsec, mainly in declination, to align the optical nucleus with that in our 18-GHz map.

2.4 *HST* optical

We make use of an archival *HST* Wide Field and Planetary Camera 2 (WFPC2) PC1 image (*F606W* filter, single 500 s exposure) published by Fosbury et al. (1998), that shows well the structural detail of the HIC. We further processed the data using the IRAF ELLIPSE software to subtract galaxy light from the image, with a view to unveiling further features associated with the radio jet and its surroundings. We applied an astrometric correction of 1.48 arcsec, mainly in right ascension, to align the nucleus with the 18-GHz radio map. We used the IRAF SYNPHOT package to calibrate the optical flux densities of features of interest.

3 RESULTS

3.1 Radio jet

Previous radio mapping of 2152−699 that was carried out with the ATCA at 4.7 and 8.6 GHz detected the core, a knot adjacent to the HIC, and emission from the S and N lobes and their embedded hotspots (Fosbury et al. 1998). In addition, VLBI has measured embedded components in the core at 8.4 GHz (Tingay et al. 1996) and the S hotspot at 1.4 GHz (Young et al. 2005). Our new map (Fig. 1) is well matched to the resolution of *Chandra* and is the first to track the jet through several knots on its way to the N hotspot, and we have therefore introduced labels for the components. Knot D lies adjacent to the HIC.

Intensity and polarization maps for the jet are shown in Figs 2 and 3, respectively, and discussed in Section 4.1. All the 18-GHz maps presented in this paper have a 0.35 arcsec restoring beam. Results for the hotspots are presented in Section 3.4. and discussed in Section 4.3.

Radio measurements are compiled in Table 1. For compact features the parameters are those of elliptical Gaussians fitted using the

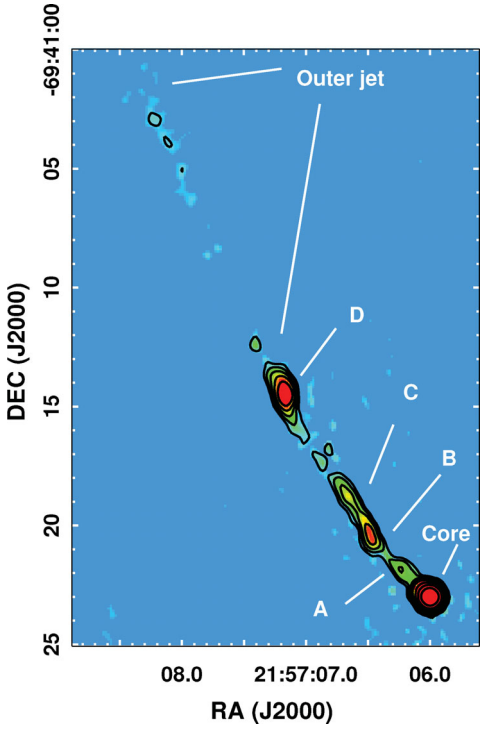

Figure 2. Expanded view of the jet at 18 GHz from the map of Fig. 1. Contours at (1, 2, 4, 8, 16, 64, 256, 1024) × 0.09 mJy beam^{-1}.

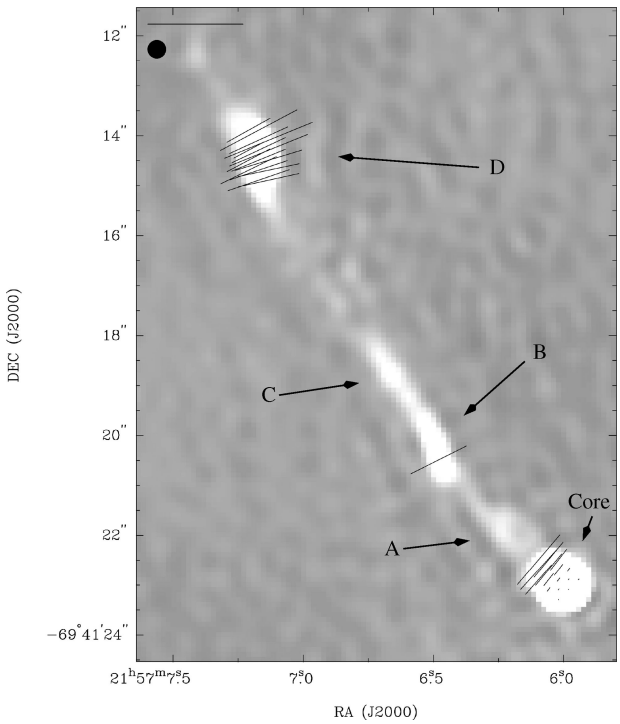

Figure 3. Inner jet shown with its fractional polarization E vectors. The scale bar at top left corresponds to 46.5 per cent polarization. The beam size is also shown at the top left.

MIRIAD task IMFIT. The tabulated polarization fraction and position angle apply to the centroid of the component in question, and Fig. 3, which shows the E-field vectors, provides an indication of the range of values over the features. Radio spectral indices have been estimated for the brightest components within the 16–20 GHz band of the observations. These are rather uncertain, to at least ±0.1, since we do not always see a smooth spectrum over our 16 subbands of frequency, presumably due to calibration errors associated with the time-variable delays present in the data.

Fosbury et al. (1998) report that between 4.7 and 8.6 GHz the core spectrum is inverted and may show some historic variability, and our 18-GHz flux density is indeed higher than at 4.7 and 8.6 GHz. We find the morphology to be complex, which is not unexpected given that VLBI finds a core–jet structure with a resolved core (Tingay et al. 1996). We have fitted the 18-GHz core (Fig. 2) to an unresolved component and a weak jet component found to be centred 0.35 arcsec away. There is marginal evidence that the core is slightly elongated in the counterjet direction, with a component ∼0.1 arcsec away, although observations with fuller baseline coverage would be required for confirmation.

A good fit to knot D requires three components. Two of these (D-1 and D-2) have position angles consistent with the overall jet direction at D, but the third (D-peak) is inclined by about 10°, in a direction closer to north–south. Interestingly, the polarization vector tilts together with the component orientation, leading to the overall spread in vectors seen in Fig. 3. The 18-GHz spectrum of the total emission from knot D appears to be rather steep, as noted by Fosbury et al. (1998) for lower frequencies. However, the D-peak subcomponent is distinctly flatter in radio-to-optical spectrum (Section 3.2).

3.2 Optical jet

As seen in the right-hand panel of Fig. 4, the galaxy-subtracted *HST* image shows not only emission in the region of the HIC, interpreted as ionized gas by Tadhunter et al. (1987, 1988) and Fosbury et al. (1998), but also emission associated with radio knot D. The optical emission is more compact than radio knot D as a whole, and the centroid gives an excellent match to the position of subcomponent D-peak. We measure a flux density at 4.97×10^{14} Hz of 2.5 ± 0.2 μJy. The interpolated 18 GHz to optical spectral index is then $\alpha_{ro} \sim 0.76$.

Diffuse optical emission along radio components B and C is also seen, totalling 2.0±0.2 μJy. Here the interpolated 18 GHz to optical spectral index is $\alpha_{ro} \sim 0.82$. Although the galaxy subtraction leads to some image artefacts, such as the triangular feature at the nucleus, the patchiness of optical emission close to the nucleus is most likely real and caused by dust obscuration. There is a significant feature immediately to the south of radio knot B. The inner V-shaped emission opening out in the jet direction may be an edge-brightened ionization cone.

3.3 X-ray jet

The left-hand panel of Fig. 4 shows an X-ray excess over background in the bright nucleus, knots B, C and D, and the HIC. The nuclear emission is the subject of a paper in preparation by Momtahan et al. In this section we concentrate on the emission associated with the radio knots, and results for the HIC are included in Section 3.5.

There are ∼100 net counts (0.3–7 keV) from knot D over all three exposures. The 18-GHz map is of a beam size well matched to *Chandra*, and the centroid and concentration of X-ray counts make it most plausible that the emission arises primarily from D-peak. Using a nearby region to measure the background ('near-bkg' in Fig. 5), and fitting using the XSPEC CSTAT statistic to a

Table 1. Parameters for radio components.

(1) Component	(2) RA, Dec.	(3) $S_{18\,\mathrm{GHz}}$ (mJy)	(4) FWHM (arcsec)	(5) PA (°)	(6) P per cent	(7) χ (°)	(8) α_r
Core	21:57:06.000 ± 0.0002, −69:41:23.001 ± 0.001	829 ± 15	–	–	0.6	−38	–
Core–jet	21:57:06.049 ± 0.002, −69:41:22.76 ± 0.01	28.3 ± 1.2	0.18 × 0.15	–	20	−38	–
Core–counterjet[a]	21:57:05.996 ± 0.006, −69:41:23.07 ± 0.04	33 ± 19	0.18 × 0.18	–	0.4	−38	–
Core-total	–	893 ± 16	–	–	–	–	0.15
A	21:57:06.227 ± 0.014, −69:41:21.91 ± 0.06	3.0 ± 0.3	1.3 × 0.6	49 ± 9	–	–	–
B	21:57:06.480 ± 0.003, −69:41:20.41 ± 0.04	4.7 ± 0.3	1.1 × 0.1	20 ± 2	30	−60	–
C	21:57:06.655 ± 0.010, −69:41:18.82 ± 0.08	3.8 ± 0.3	1.8 × 0.2	33 ± 2	–	–	–
D-1	21:57:07.194 ± 0.003, −69:41:14.63 ± 0.05	5.0 ± 0.7	1.7 × 0.2	24 ± 2	30	−65	–
D-peak	21:57:07.164 ± 0.001, −69:41:14.57 ± 0.01	5.9 ± 0.5	0.4 × 0.1	8 ± 3	30	−73	–
D-2	21:57:07.168 ± 0.004, −69:41:14.14 ± 0.05	4.7 ± 0.5	0.8 × 0.2	26 ± 3	30	−65	–
D-total	–	15.6 ± 1	–	–	–	–	1.4
N-hotspot-peak	21:57:09.932 ± 0.003, −69:40:39.56 ± 0.01	25.6 ± 0.8	0.7 × 0.5	79 ± 9	30	+48	0.7
N-hotspot-total	–	50.5 ± 2	–	–	–	–	1.4
S-hotspot-peak	21:57:04.112 ± 0.003, −69:41:46.66 ± 0.02	68 ± 3	0.5 × 0.3	−3 ± 22	50	−80	0.7
S-hotspot-tip	21:57:03.926 ± 0.007, −69:41:50.21 ± 0.02	5.9 ± 0.4	0.8 × 0.3	−73 ± 8	27	+7	–
S-hotspot-total	–	223.9 ± 10	–	–	–	–	1.5

Notes. (1) Component name. Three subcomponents combine to make the flux density of each of the core and component D. For each hotspot the total flux density within the 90 μJy beam^{-1} contour and that in the brightest, most compact, component are reported separately. (2) J2000 position. The relative coordinates have random errors as quoted, but the absolute accuracy is uncertain by ±(0.″007, 0.″04) based on the phase referencing to B2353−686. (3) Total 18-GHz flux density in component. (4) Deconvolved FWHM of Gaussian major and minor axes. (5) Major axis position angle. (6) Polarization percentage. (7) Polarization position angle of the electric vector. See Figs 3, 7 and 11 to gauge the uncertainties in the polarization. (8) Spectral index between 17 and 19 GHz. Uncertain due to inconsistencies with indices within the two subbands, presumably caused by the time-variable phase gradients.

[a]Significant improvement to residuals when component included in the complex core structure, but only marginal evidence that this flux density is associated with a separate component.

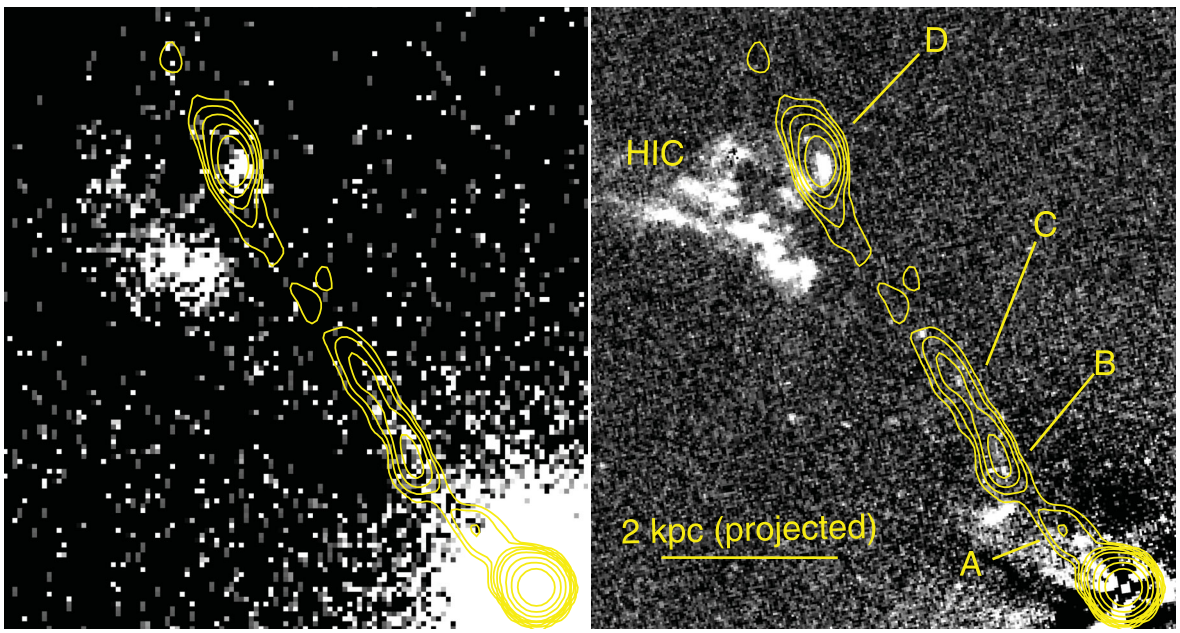

Figure 4. Left: 0.5–2.5 keV exposure-corrected unsmoothed image (0.0984-arcsec pixels) with radio contours from Fig. 2. The deficit of counts on a line from the core to the S of the HIC is due to removal of the readout streak from the core. Right: *HST F606W* image (0.046-arcsec pixels) after galaxy subtraction using the IRAF ELLIPSE routine. The triangular feature at the core is an artefact, but the inner V-shaped emission opening out in the jet direction may be an edge-brightened ionization cone. The optical emission just to the S of knot B is believed to be real, and the patchiness near the core is likely to be due to obscuration from dust. Both the X-ray and optical show emission from knot D, and fainter emission tracking the jet mid-line at B and C.

power-law model with Galactic absorption, we find a 1 keV flux density of 1.3 ± 0.3 nJy and a spectral index of $\alpha_\mathrm{x} = 1.2 \pm 0.4$, which is in agreement with the more poorly constrained result of Young et al. (2005) for ObsId 1627 based on hardness ratio. The 0.3–5 keV luminosity is 1.3×10^{40} erg s^{-1}. ObsId 1627 used the S3 chip and occurred before the build up of contaminants that have affected *Chandra*'s low-energy response, and so detected more counts than would be expected from a direct scaling with exposure time. Curiously there are twice the number of net counts in ObsId 11530 (57) as in ObsId 12088 (28). Although this appears to be marginally

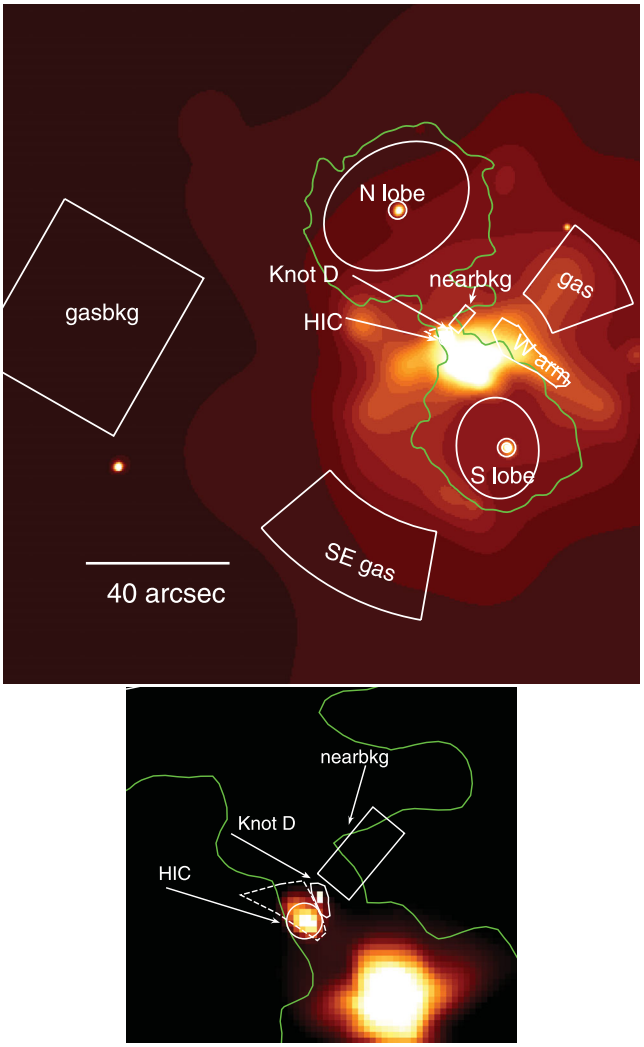

Figure 5. 0.5–2.5 keV exposure-corrected and adaptively smoothed (3σ threshold) *Chandra* image of 2152−699, outlining in white some of the regions used for spectral extraction. The lowest radio contour from the map of Fig. 15 is shown in green. The circles within the lobes mark the hotspot regions: in the case of the S lobe the larger circle marks the excluded region for extracting lobe counts, and the smaller circle is used to extract the peak of the hotspot emission. Lower panel shows an expanded view of the inner regions: the HIC is marked by both a dashed polygon and a circle covering its brightest emission to the south-west.

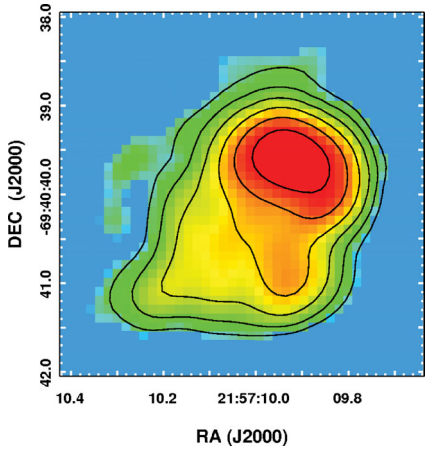

Figure 6. Expanded view of the northern hotspot from the map of Fig. 1. Contours are at (1, 2, 4, 8, 16, 32) × 0.11 mJy beam^{-1}. The area within the 90 μJy beam^{-1} contour is 6.6 arcsec^2.

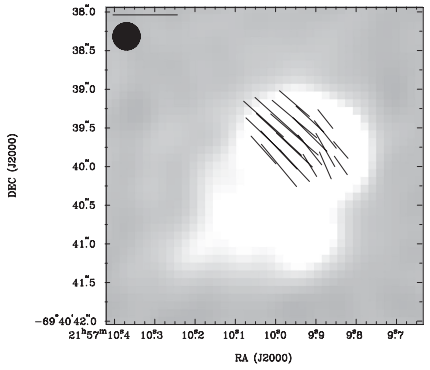

Figure 7. North hotspot shown with its fractional polarization E vectors. The scale bar at top left corresponds to 34.7 per cent polarization. The beam size is also shown at the top left.

significant it is not readily understood: D-peak is resolved in the radio (Table 1), and the X-ray luminosity is sufficiently high that significant contamination from a variable X-ray binary in the host galaxy is unlikely. The roll angles of the two observations differ by less than an arcsecond, and knot D is sufficiently far from the read-out streak (see Fig. 4) that its counts are unaffected by the streak. The discrepancy in counts is only significant above 1 keV, where it shows up mostly where the spectral sensitivity is highest at 1–2 keV. We disregard any variability in what follows and attribute the average flux to non-thermal emission from D-peak. We note that the X-ray emission from knot D is significantly harder than that in the HIC (see Section 3.5), and an attempt to fit a thermal model finds an unrealistically high temperature of $kT \sim 2.3$ keV.

The net counts in knots B and C are measured using an adjacent background region to the north-west (so avoiding readout streaks to the south-east in ObsIds 11530 and 12088). We find only 45 ± 10 counts (0.3–7 keV) over the three observations, which is too few for useful spectral fitting. An estimate of the luminosity of the emission can be obtained through scaling values for knot D by the net counts (see above), on the assumption that the spectral shape is similar.

3.4 Hotspots

Radio, X-ray and optical images for the N and S hotspots are shown in Figs 6–13. 18 GHz measurements appear in Table 1. While the total hotspot spectra are unusually steep at 18 GHz, as commented also by Fosbury et al. (1998) for lower frequencies, the peaks of the emission have more normal spectral indices of $\alpha_r \sim 0.7$ (Table 1). Our measurements for the peak of the S hotspot are consistent with roughly one-third of its flux density being contributed by the VLBI components of Young et al. (2005) (unresolved in our beam), if we extrapolate between 1.4 and 18 GHz using $\alpha_r = 0.7$.

The X-ray emission in the N hotspot (Fig. 8) is clearly offset from the radio peak: its centroid is 1.14 arcsec (∼600 pc) from the peak of the radio emission. The X-rays are strong where the jet must be entering from the S and where the radio emission is of steeper spectrum than in the peak. This is in marked contrast to the X-ray emission in the S hotspot (Fig. 12) which shows good agreement between the X-ray and radio peaks. For the N hotspot we have fitted the ∼100 net X-ray counts in a circle of radius 2.5 arcsec centred on the radio peak to a power law using region 'N lobe' (Fig. 5) as

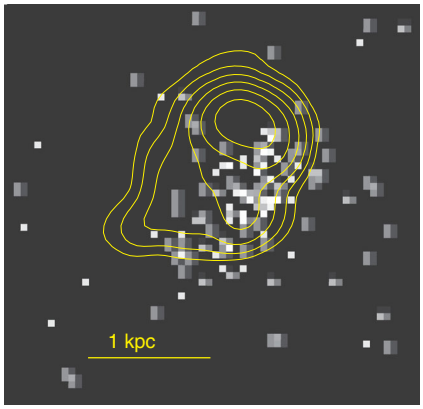

Figure 8. 0.3–5 keV exposure-corrected unsmoothed image (0.0984-arcsec pixels, log scaling, individual counts shown) of the N hotspot, with radio contours from Fig. 6. The X-rays are bright where the jet enters the hotspot, offset from the peak of the radio emission.

background. The 1-keV flux density is 1.0 ± 0.2 nJy and $\alpha_x = 0.8 \pm 0.3$. For the S hotspot we have fitted the ∼100 net X-ray counts in a circle of radius 1.25 arcsec centred on the radio peak to a power law using region 'S lobe' (excluding a region of radius 2.5 arcsec around the hotspot) as background (Fig. 5). The 1-keV flux density is 1.25 ± 0.25 nJy and $\alpha_x = 1.0 \pm 0.3$.

The WFI observation finds optical emission associated with each of the N and S hotspots (Figs 9 and 13). Within apertures of radius ∼1.5 arcsec the flux densities at 5.5×10^{14} Hz are 2^{+2}_{-1} and 4^{+4}_{-2} μJy for the N and S, respectively, with the errors dominated by the dispersion when using different apertures and methods for background subtraction. To determine if the hotspot optical emission is resolved we first fitted Gaussians to nearby stars, finding an average FWHM of 2.43 ± 0.02 arcsec. For the N hotspot, the fitted position is $\sim 0.4 \pm 0.2$ arcsec to the south of the radio peak, and the deconvolved size of the optical emission is $(2.4 \pm 0.4) \times (1.7 \pm 0.5)$ arcsec. The optical is thus mostly emission from the radio peak, with some originating from the X-ray bright region to its south. For the S hotspot, the fitted position of the optical emission agrees within errors with that of the peak of the radio emission, and the deconvolved size is $(1.8 \pm 0.4) \times (1.1 \pm 0.6)$ arcsec. Here the X-ray and optical are both dominated by emission from the radio peak.

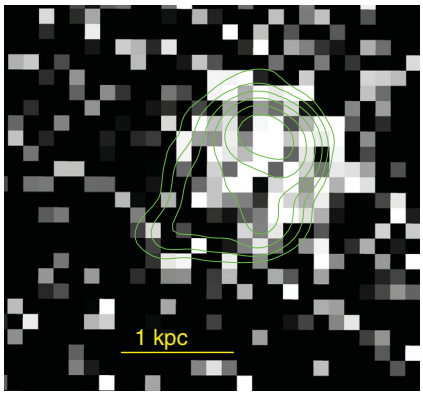

Figure 9. WFI optical image (0.24-arcsec pixels, log scaling) of the N hotspot, with radio contours from Fig. 6. The optical is brightest close to the peak of the radio emission, but is also somewhat elongated along the X-ray excess to the S.

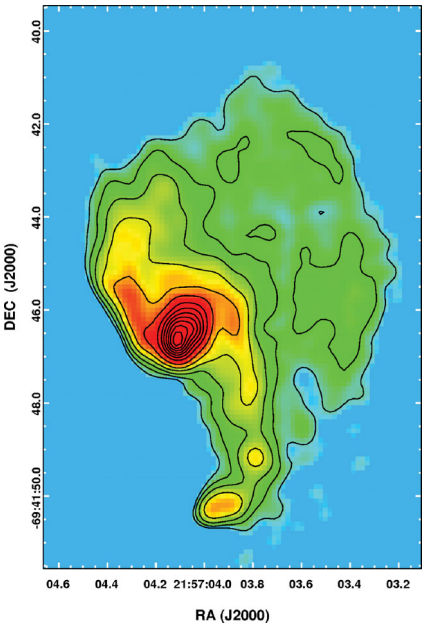

Figure 10. Expanded view of southern hotspot from the map of Fig. 1. Contours are at (1, 2, 4, 8, 16, 32, 64, 96, 128, 160, 192, 224, 256) × 0.095 mJy beam^{-1}. The area within the 90 μJy beam^{-1} contour is 38.3 arcsec^2.

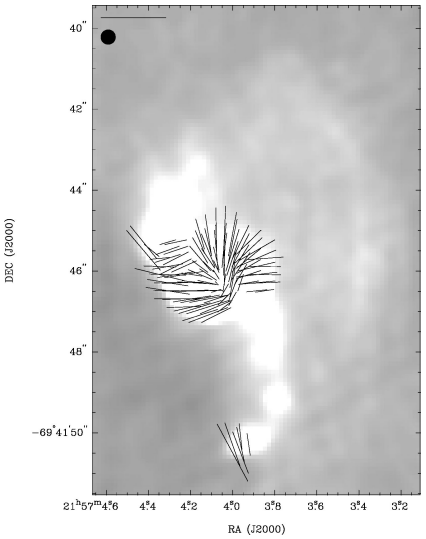

Figure 11. South hotspot shown with its fractional polarization E vectors. The scale bar at top left corresponds to 87 per cent polarization. The beam size is also shown at the top left.

3.5 The HIC

We have fitted models to the spectrum of the ∼429 net X-ray counts in an area of 5.3 kpc^2 at the HIC, using the on-source (dashed) and background regions labelled 'HIC' and 'nearbkg', respectively (Fig. 5). Essentially all the detected emission is below 3 keV. A fit to a power-law model is only marginally acceptable, and gives an unrealistically steep spectral index of $\alpha_x \sim 3.2$. A thermal model fits well, with $kT \sim 0.29$ keV. What is striking, however, is the low metallicity of the gas relative to solar ($Z/Z_\odot$), with values less than a few per cent. This is not true of other thermal components in the field (see Section 3.6). Confidence contours in kT and abundance are shown in the left-hand panel of Fig. 14. Abnormally low

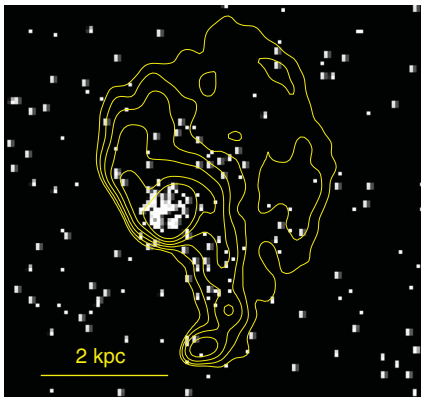

Figure 12. 0.3–5 keV exposure-corrected unsmoothed image (0.0984-arcsec pixels, log scaling, individual counts shown) of the S hotspot, with the six lowest radio contours from Fig. 6. The X-rays are brightest at the peak of the radio emission.

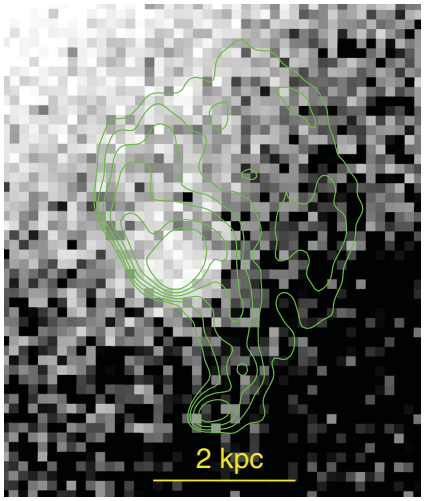

Figure 13. Optical image (0.24-arcsec pixels, log scaling) of the S hotspot from the WFI, with the six lowest radio contours from Fig. 6. Like the X-ray, the optical is brightest at the peak of the radio emission. The optical emission to the north-east is galaxy light.

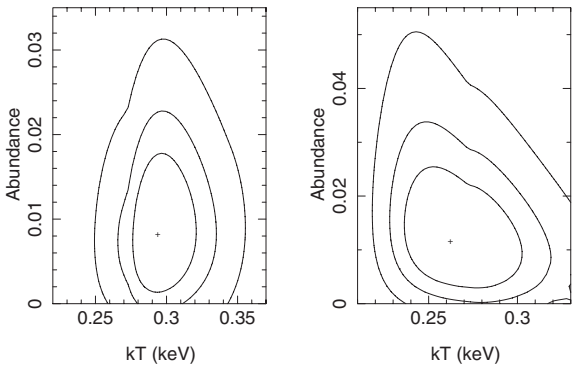

Figure 14. Confidence contours (1σ, 90 and 99 per cent for two interesting parameters) for kT and abundance ($Z/Z_{\odot}$) for a thermal model fitted to the spectral data from the HIC. Left: thermal model only. Right: a thermal bremsstrahlung model has been added to allow for a contribution from X-ray binaries.

abundances can result from neglecting to account for a component of unresolved low-mass X-ray binaries (LMXB). We have tested that in the HIC by applying the method used by Humphrey et al. (2009) and Worrall et al. (2010) for other local radio galaxies of adding in a thermal-bremsstrahlung model of free normalization but fixed $kT = 7.3$ keV, the well-constrained best fit for 15 nearby early-type galaxies from Irwin, Athey & Bregman (2003). The best-fitting 0.3–5 keV luminosities are then 10^{41} and 7×10^{39} erg s^{-1} for the thermal gas and LMXBs, respectively. Uncertainties in the thermal bremsstrahlung normalization are large, and the best-fitting value is almost certainly an overestimate since the HIC covers only a small area of the galaxy and the *total* luminosities from LMXBs in 14 early-type galaxies are derived by Kim & Fabbiano (2004) to lie in the range a few $\times 10^{39}$ to several $\times 10^{40}$ erg s^{-1}. However, the effect of the inclusion of a LMXB component on the fitted parameters for the thermal gas is small (see right-hand panel of Fig. 14), and the normalization of the thermal component is reduced by less than 5 per cent. In particular the gas metallicity is still constrained to be low, and an X-ray binary component is not considered further.

A circle of radius 1.5 arcsec (0.85 kpc) centred on RA = 21:57:07.408, Dec. = −69:41:16.53 contains 88 per cent of the HIC net X-ray counts. Parameter values for a fit to a thermal model are essentially the same as in Fig. 14 (left-hand panel), with the contours slightly larger due to fewer counts. Since the X-ray emission from the HIC extends further, particularly to the north-east, it is unlikely that the most intense emission arises from an unresolved feature, and we treat 1.5 arcsec as the effective angular radius of this complicated region in estimating gas density and pressure in Section 4.4. The bolometric luminosity of the X-ray component in this circular extraction region is 3.3×10^{41} erg s^{-1}.

3.6 The large-scale gas distribution

The most striking features of the larger scale X-ray gas distribution are arms around the lobes, particularly in the south, where there is a clear gas cavity associated with the radio emission (Fig. 15). Here the lobe is embedded in gas, whereas the N lobe appears not to be capped by bright gas at its N extremity. The overall appearance in the highest surface brightness X-ray emission is that of a truncated figure of eight.

We have fitted spectral models to gas in regions indicated in Fig. 5. 'W Arm' covers the brightest part of the arm around the southern radio lobe. The region labelled 'gas' is a section of a core-centred annulus which was chosen on the basis of intensity and morphology to represent the location of undisturbed gas. We have also applied spectral fitting to the weaker emission from a core-centred annulus labelled 'SE gas', lying to the south-east of the southern lobe. Checks were made to verify that results were insensitive to the precise selection of a local background region (taken to be no closer to the nucleus than 'SE gas'), and results presented here use the region labelled 'gasbkg'. All the regions lie fully on the S3 chip for ObsId 1627 and the I3 CCD for ObsIds 11539 and 12088, and avoid the readout streak from the core and serendipitous X-ray sources found using the CIAO WAVDETECT task.

The wings of the point spread function (PSF) of the bright nucleus supply position-dependent X-ray emission that it was found necessary to model, since on-source and background regions were from different off-axis angles. As the central pixels of the nucleus suffer from pile-up, we used measurements from the read-out streak (see Momtahan et al., in preparation, for details) to characterize the spectrum that was used in a 2-million-second simulation of the PSF

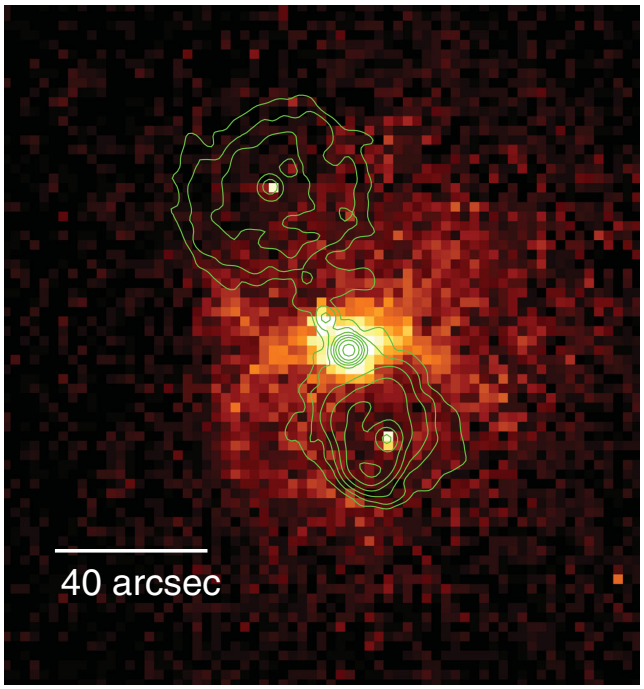

Figure 15. 0.5–2.5 keV exposure-corrected unsmoothed *Chandra* image in 2.5-arcsec bins. Contours are from the 4.74-GHz data of Fosbury et al. (1998), mapped with a 2.35 arcsec restoring beam. Levels are (1, 2, 4, 8, 16, 32, 64, 128) × 3 mJy beam^{-1}.

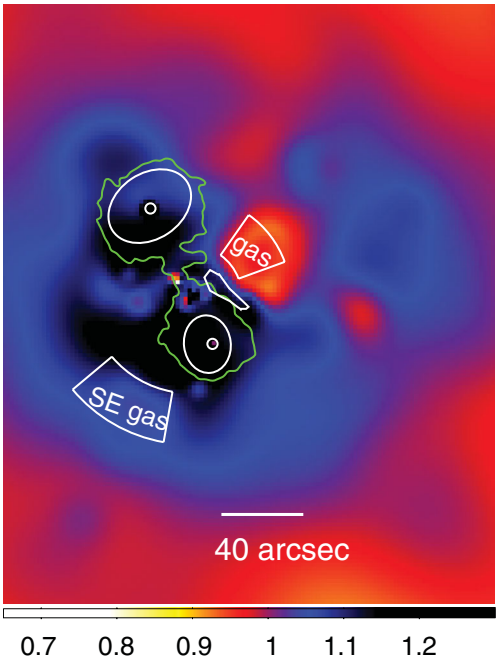

Figure 16. X-ray temperature map made following the prescription and correlation between mean photon energy and temperature of David et al. (2009). The colour bar is a rough indicator of kT in units of keV. Adaptive smoothing at 3σ threshold has been applied after blocking the data to a pixel size of 1.968 arcsec. The lowest radio contour from the map of Fig. 15 is shown in green, together with the locations of several regions from Fig. 5.

with Chandra Ray Tracer (ChaRT) at the location of the nucleus in the long ACIS-I observations. We then used MARX to create an event file from which spectra could be extracted and fitted using on-source and background regions at the same locations relative to the optical axis as apply to the data from 2152−699. Fits of the spillover counts from the wings of the simulated PSF to single-component power laws were acceptable for all the regions described above. The results were included in spectral models applied to the 2152−699 data as fixed-parameter power-law components. Including the PSF wing component caused the 0.3–5 keV luminosity of the thermal gas emission to decrease by 24 per cent in 'W Arm', but the effect was smaller elsewhere.

All three regions described above then gave an acceptable fit to a single-component thermal model (Table 2). When we take into account the fact that the quoted errors are roughly equivalent to 90 per cent confidence on a single parameter, we see there is less than 1 per cent chance of emission in 'W Arm' being at the same temperature as that in the 'gas' region. The 'SE gas' also appears cooler than 'W Arm', although at lower confidence due to the reduced intensity of this emission.

Table 2. X-ray spectral fits to non-lobe gas emission.

Region	Thermal			χ^2/dof
	kT (keV)	$Z/Z_\odot$	N (equation 1, cm^{-5})	
W Arm	$1.33^{+0.27}_{-0.11}$	$0.31^{+0.60}_{-0.16}$	$(2.5 \pm 1.0) \times 10^{-5}$	19.4/17
Gas	$0.95^{+0.05}_{-0.06}$	$0.37^{+0.42}_{-0.17}$	$(2.7^{+1.4}_{-1.2}) \times 10^{-5}$	22.5/26
SE gas	1.00 ± 0.25	$0.07^{+0.13}_{-0.06}$	$(3.3^{+2.5}_{-1.2}) \times 10^{-5}$	16.1/18

Notes. Regions are from Fig. 5 with 'gasbkg' sampling the background. Errors are 1σ for two interesting parameters. Absorption is consistent with the Galactic value and fixed. A fixed-parameter power-law component based on simulations has been included to account for the wings of the PSF from the nucleus.

We checked how the results for the thermal gas would be affected by including a contribution from unresolved LMXBs, as described in Section 3.5. As compared with Table 2, for 'W Arm' kT is only marginally affected and constrained to lie between 1.19 and 1.48 keV, the abundances are now poorly constrained at the high end, and the normalization (which is not used in subsequent discussion) should be reduced by about 8 per cent (or more if the gas abundance is truly anomalously high). In the other regions the effect is also to decrease slightly kT (to lie between 0.88 and 0.99 in the case of 'gas') and the abundances are similarly affected. Here the normalizations in Table 2 are affected by a negligible amount for the abundances quoted. The conclusion that the emission from 'W Arm' is hotter than in the other regions is therefore unaffected by a relatively small, but uncertain, contribution from unresolved LMXBs.

In an attempt to probe the overall temperature distribution of the gas we have applied the method of David et al. (2009) to produce an image that represents the gas temperature. This method exploits the fact that the L-shell line emission from thermal gas of $kT \sim 1$ keV is blended into a broad peak whose centroid energy shifts to higher values as the temperature increases, and is applicable for gas with kT roughly in the range 0.7–1.2 keV. The method involves producing an image of the mean energy of photons in the event file as a function of position, and the image is subsequently smoothed for display (Fig. 16). A limitation of the method is that since it works on individual events, no background is removed, and so the background needs to be uniform in intensity and spectrum across the field to avoid biasing the results. In the case of 2152−699 this is not the case for the contribution from the wings of the PSF, and so we use the results here only in a qualitative way, and have applied

Table 3. X-ray spectral fits to lobe emission.

Region	Power law		Thermal		χ^2/dof
	α_x	1 keV normalization ($cm^{-2}\,s^{-1}\,keV^{-1}$)	kT (keV)	N (equation 1, cm^{-5})	
S lobe	0.90 ± 0.24	$(7.3 \pm 1.1) \times 10^{-6}$	–	–	27/23
N lobe	$0.88^{+0.46}_{-0.72}$	$(6 \pm 4) \times 10^{-6}$	$1.2^{+0.4}_{-0.2}$	$(1.3 \pm 1.0) \times 10^{-5}$	27/31

Notes. Regions are from Fig. 5 with hotspots excluded and 'gasbkg' sampling the background. Errors are 1σ for two interesting parameters. Absorption is consistent with the Galactic value and fixed. Thermal fits are insensitive to abundances which are fixed at $0.3\,Z_\odot$.

the calibration of mean energy to kT of David et al. (2009) rather than attempting a calibration for this particular field. Nevertheless, the results are enlightening. In particular Fig. 16 shows that the region labelled 'gas', that was picked to represent undisturbed gas purely on the basis of X-ray intensity and its location with respect to the radio lobes, appears strikingly cool compared with surrounding emission. Indeed the temperature structure to the west of the radio source appears to be more disturbed than that to the east.

3.7 X-ray emission from the lobes

We have extracted the X-ray emission from the N and S lobes, using the regions shown in Fig. 5, with the larger of the inner circles used as hotspot exclusion zones. Local background was measured from the region marked 'gasbkg', and the contribution from the wings of the nuclear PSF was included in model fitting as described in Section 3.6. When the emission from the S lobe was fitted to a thermal model, the temperature was high compared with other regions (Table 2), at $kT \sim 5$ keV. A fit to a power law (Table 3) is equally acceptable, finding a spectral index in agreement with that of the low-frequency radio emission of $\alpha_r = 0.8$ (Kühr et al. 1981). When thermal bremsstrahlung, to accommodate possible emission from unresolved LMXBs, was included, its normalization tended to zero. It is therefore most likely that the X-ray emission is dominated by inverse Compton scattering of the cosmic microwave background (CMB) radiation by the population of electrons responsible for the radio emission.

The situation in the N lobe is more complex. Again a fit to a thermal model gave a higher temperature than other gas in the field, but a power-law model gives a spectrum that is significantly steeper than the radio. The radio surface brightness is lower than in the S lobe, and the extraction region needed to be larger to get >500 net counts. The larger region is expected to include significantly more thermal gas surrounding the lobe than in the brightest part of the S lobe where the thermal contribution appears to be negligible. A combination of a power law and thermal model not only gave an improved fit ($\Delta\chi^2 = 5$) but more sensible best-fitting parameters given the overall source characteristics (Table 3).

For application of an inverse Compton model we have assumed that the X-ray spectral index matches the radio, in which case the measurements of 1 keV flux density, with 1σ errors, are 4.6 ± 0.3 and 3.5 ± 0.7 nJy for the non-thermal component in the S and N lobes, respectively.

4 DISCUSSION

4.1 The jet morphology

The new 18-GHz data reveal the polarization structure and path taken by the jet from the core on its way to the N hotspot. As is often the case in radio galaxies (e.g. Saikia 1999; Jorstad et al. 2007), the core is of low radio polarization, but after ∼0.35 arcsec the polarization has jumped to ∼20 per cent, with an implied magnetic field direction along the jet. Through component A the jet continues in its VLBI direction, heading towards the HIC. As pointed out by Tadhunter et al. (1988) and Fosbury et al. (1998), the direction supports suggestions that the HIC is at least partially photoionized by beamed emission from the inner jet. We now know this inner jet extends in the required direction for a projected distance of ∼1.5 kpc. The inner V-shaped emission seen in the *HST* data (Fig. 4, right) may be an edge-brightened ionization cone similar to that seen in, for example, NGC 1068 (Unger et al. 1992).

The data then show the jet deflection to be complicated. In component B there is significant clockwise bending, accompanied by realignment of the magnetic field to maintain its dominant alignment along the jet. The new angle would take the jet straight to the N hotspot, except that the jet deflects anticlockwise in component C. Diffuse optical and X-ray emission are seen along knots B and C. In component D, the brightest jet knot, the jet deflects back clockwise to the angle required to reach the N hotspot. It passes through the misoriented subcomponent, D-peak, towards the leading edge of the brightest emission in D. D-peak has the curious property of being misaligned relative to the rest of component D in position angle and polarization angle (Table 1). Optical and X-ray emission in knot D appear to be associated principally with D-peak, giving an interpolated 18 GHz to optical spectral index of $\alpha_{ro} \sim 0.76$, which is flatter than the radio spectrum integrated over all of knot D. On leaving component D the jet is much fainter and on a path towards the N hotspot. Further multiple deflections are not required but cannot be excluded.

It is an interesting question as to why the jet takes a zigzag path through components A, B, C and D. The discovery of optical emission at the base of knot B, where the first such bending occurs, may be relevant. The optical feature at the base of knot B has similar surface brightness to the HIC, which lies adjacent to knot D where more bending occurs. If this comes from a finger of gas that is pushing the jet and causing the deflection, spectroscopic measurements of line widths should measure momentum transfer to the jet. Jet deflection in knot C is less pronounced than in B and D, and there is no bright feature in the *HST* image that might signal the presence of excited gas there.

Our new radio measurements help to address the important, but uncertain, angle to the line of sight, θ, and bulk flow speed, βc. Use of the brightness ratio between approaching and receding jets (e.g. Bridle & Perley 1984), R_j, rests on the assumption that internal and external factors are the same on each side of the core. This is not true for 2152−699 on large scales, since the receding jet to the south has disrupted closer to the core and produced a brighter hotspot and 18-GHz lobe. If we nevertheless apply the test to the inner jet at knots B and C, we measure $R_j > 15$, from which we infer that $\beta \cos\theta > 0.45$ for an adopted spectral index of $\alpha_r = 0.8$. The nuclear optical spectrum, of intermediate ionization and exhibiting both forbidden

and permitted lines with broad wings, is described by Tadhunter et al. (1988) as similar to that of Pictor A, a well-studied, somewhat more powerful, radio galaxy at $z = 0.035$. Marshall et al. (2010) conclude that Pictor A's jet most likely lies at $10^\circ < \theta < 45^\circ$, as a lobe-dominated object whose nuclear optical spectrum should be accommodated by unification models, and it is reasonable to adopt the same argument for 2152−699. The radio core prominence of 2152−699 is also comfortably within the range typical of broad-line objects, but not extreme (e.g. its value of 5×10^{-3} can be compared with those for different source types in fig. 7 of Hardcastle et al. 2004). When the constraint on θ is combined with the constraint on $\beta \cos\theta$, the relativistic Doppler factor, $\delta = \sqrt{1-\beta^2}/(1-\beta\cos\theta)$, is also constrained. If $\theta = 10^\circ$, δ for the jet is permitted to take on its largest value, and largest range of values, being constrained to lie between 1.6 and 5.7 (corresponding to $\beta = 0.46$ and 0.98, respectively). At $\theta = 45^\circ$, the maximum allowed value of δ is 1.4, corresponding to $\beta = 0.64$, and δ is lower for faster bulk flows. Under all these conditions, the counterjet is constrained to have $\delta < 0.6$ (<0.5 if $\theta = 45^\circ$).

4.2 The jet knots

Fig. 17 shows the multiwavelength spectrum of knot D-peak modelled with a broken power law. The lower frequency radio measurements of Fosbury et al. (1998) are also plotted, but these contain emission from the whole of knot D and some lobe emission. The spectrum of slope $\alpha_{\rm ro} = 0.76$ must break if it is to extrapolate as a single component to the X-ray: a similar result applies to knots B/C. This is as expected for synchrotron radiation from a single power-law distribution of electrons if energy losses are responsible for the break. A simple energy-loss model predicts $\Delta\alpha = 0.5$, in which case the break arises at $\sim 8 \times 10^{14}$ Hz in knot D-peak, as plotted. However, larger breaks are often observed in low-power FRI jets (e.g. Böhringer et al. 2001; Hardcastle, Birkinshaw & Worrall 2001; Birkinshaw, Worrall & Hardcastle 2002), in which case the break frequency will be somewhat higher. The X-ray spectral index of $\alpha_{\rm x} = 1.2 \pm 0.4$ is consistent with the extension of a broken power law, although is insufficiently well measured to immediately rule out an inverse Compton origin, for which the spectral slope must match that of the radio synchrotron emission of the responsible electrons.

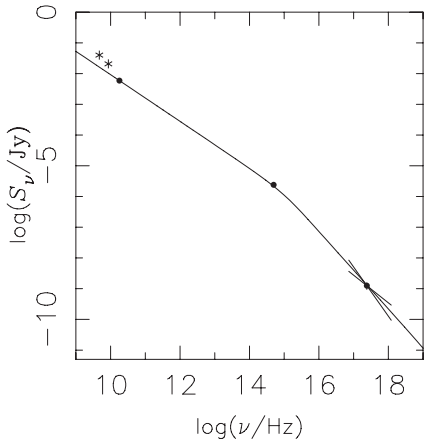

Figure 17. The radio–optical–X-ray spectral distribution in knot D-peak is consistent with a broken power law arising from a single-component electron spectrum emitting synchrotron radiation, with energy losses being significant at the higher frequencies. The two lowest frequency radio points are from Fosbury et al. (1998) and include emission over a larger region.

We model the radio component D-peak as a cylinder of length 0.4 arcsec and radius 0.05 arcsec (Table 1). We find a minimum-energy magnetic field of $B_{\rm me} \sim 46$ nT for a fully leptonic plasma whose electron spectrum extends with spectral index of $2\alpha_{\rm ro} + 1 = 2.52$ down to a Lorentz factor of $\gamma_{\rm min} = 10$, and where the bulk relativistic Doppler factor is $\delta = 1$ (for relevant equations see e.g. Worrall & Birkinshaw 2006). The B/C region, modelled as a cylinder of length 3.3 arcsec and radius 0.1 arcsec, with a spectrum of $\alpha_{\rm ro} = 0.82$ to connect the 18 GHz and *HST* data points, gives $B_{\rm me} \sim 20$ nT. If there is significant relativistic beaming (see Section 4.1) and we treat this as a steady jet, the values of $B_{\rm me}$ should be divided by $\delta^{(2+\alpha_{\rm ro})/(3+\alpha_{\rm ro})}$.

The X-ray emission in quasar jets at small angle to the line of sight is frequently modelled as arising from inverse Compton scattering of CMB radiation that is boosted in the rest frame of a fast jet having a minimum-energy magnetic field (for a review see Worrall 2009). For galaxy-scale jets, starlight can be more important than the CMB for such scattering (e.g. Celotti, Ghisellini & Chiaberge 1991; Stawarz, Sikora & Ostrowski 2003). We have fitted 2152−699's starlight distribution, taken from our WFI data, to a Sérsic profile, and derived the bolometric surface-brightness profile using the total V-band magnitude given by De Vaucouleurs et al. (1991) and the bolometric correction appropriate for a K2 star. We deprojected the profile to estimate the bolometric volume emissivity of starlight, and integrated to find the local energy density as a function of position in the galaxy. We find that the X-ray inverse Compton contribution from starlight dominates over the CMB at the deprojected position of knot D only if the viewing angle $\theta > 7^\circ$. We used equation (7) of Worrall (2009), modified to include both starlight and the CMB, to calculate the beaming parameters required to produce the X-ray emission. We find that sufficient X-ray emission is produced only if knot D lies at $\theta < 2^\circ$ (i.e. CMB-dominant scattering) with very large Doppler factors (e.g. $\delta \approx 44$ for $\theta = 1^\circ\!.3$). The values are implausible for a radio galaxy and are well outside our estimates for 2152−699 (Section 4.1). While extreme bulk flow and bending into the line of sight within a single knot might be possible, X-rays are seen in other radio-bright jet regions in 2152−699, and a common origin for the X-ray would seem more plausible.

If we now proceed under the assumption that δ is close to unity, inverse Compton X-ray emission in the jet is dominated by synchrotron self-Compton (SSC) emission. At minimum energy, our modelling of both D-peak and the B/C region produces too little X-ray emission by a factor of ∼3000.

We thus conclude that the jet X-rays arise from synchrotron radiation. The electrons emitting at the spectral break, $\nu_{\rm br}$, in Fig. 17 are then of energy $E \approx \sqrt{\nu_{\rm br}/(0.1 B_{\rm me})} \approx 4 \times 10^{11}$ eV, and lose their energy in $\tau \approx 0.13/(E B_{\rm me}^2) \approx 150$ yr. Such a light travel time corresponds to an angular size of ∼0.1 arcsec, which is comparable to the radio dimensions of D-peak, supporting the idea of continuous acceleration occurring in a small region within D-peak, presumably as the result of a strong shock. A similar argument applied to B/C finds that the electrons radiating at the spectral break would lose their energy after travelling an angular distance of about 0.35 arcsec. The observation of diffuse optical emission over jet paths longer than this, particularly in knot B, requires particle acceleration from diffuse regions or a series of knots.

In contrast to FRIs, where *Chandra* synchrotron jets are common and illustrate the need for particle acceleration remote from the cores (Hardcastle et al. 2001; Worrall, Birkinshaw & Hardcastle 2001; Worrall 2009, for a review), detections of X-ray synchrotron

emission in FRII radio-galaxy jets are rare. Thus the requirement for particle acceleration within their flows (before the terminal hotspots) is not well established, except in a few cases usually associated with isolated bright knots (Wilson, Young & Shopbell 2001; Hardcastle & Croston 2005; Kraft et al. 2005; Worrall & Birkinshaw 2005; Kataoka et al. 2008). While 2152−699 is not a tremendously powerful FRII source, it certainly does not have the morphology of an FRI on either side of the core, making the evidence for diffuse particle acceleration here of particular interest.

4.3 The hotspots

Our 18-GHz data provide good imaging and polarimetry of both hotspots. While the overall spectral indices are steep, the peaks show flatter spectra (Table 1), in the range expected for particle acceleration (e.g. Achterberg et al. 2001). The N hotspot is the fainter. In the radio its intensity and polarization structure are reasonably simple. It is interesting that the brighter hotspot is that south of the core, where no jet emission is seen, and as interpreted as the side oriented most away from the observer. The southern radio lobe is also brighter and smaller, presumably due to enhanced interaction with the hot gas, as discussed in Section 4.6, and we detect some lobe emission at 18 GHz despite the small beam and high frequency. The radio structure of the S hotspot is fascinating. The appearance is that of a spiral of plasma with longitudinal magnetic field. VLBI components are embedded in this spiral (Young et al. 2005). The pattern extends to the southern tip of the hotspot, where again polarization is strongly detected.

The peak of the S hotspot is bright in radio, optical and X-ray (Figs 10–13). If we interpret the emission as synchrotron radiation in a broken power-law spectrum with $\Delta\alpha = 0.5$ (Section 4.2), we find that a power law of $\alpha_r = 0.7$, breaking to $\alpha = 1.2$ at $\sim 10^{12}$ Hz, is in reasonable agreement with the optical and X-ray measurements, including the X-ray spectral index (Fig. 18). We extrapolate the electron spectrum down to $\gamma_{\rm min} = 650$ (Godfrey et al. 2009) to find a minimum-energy magnetic field of $B_{\rm me} \sim 25$ nT for $\delta = 1$, in which case the predicted X-ray SSC emission falls below observations by a factor of ∼100. The shortfall in predicted X-ray emission is not rectified by breaking the emission into the subcomponents of Young et al. (2005), since the three subcomponents are all resolved with VLBI and are distributed fairly evenly in flux density. In order to explain the origin of the X-rays from the peak of the S hotspot as SSC emission, the magnetic field strength would need to be a factor of ∼13 lower than the minimum-energy value to provide sufficient particles for inverse Compton scattering without exceeding the observed radio flux. Such a large departure from minimum energy makes a synchrotron origin seem more likely; a better constrained X-ray spectrum could provide a definitive test. While optical hotspot detections are still fairly rare, in X-rays a synchrotron origin has been claimed for a number of hotspots, increasing in fraction as source power decreases (Hardcastle et al. 2004). As a relatively low-power FRII source, 2152−699 is consistent with such a trend.

If emission from the peak of the S hotspot is indeed synchrotron in origin, the values above with equations from Section 4.2 give a lifetime of electrons emitting at the spectral break, τ, of $\sim 10^4$ yr. This is about 10 times the light travel time across the hotspot, and acceptable as magnetic fields help to confine particles within hotspots. Perlman et al. (2010) use a synchrotron model for one of the hotspots of 3C 445 to argue that $\gamma_{\rm min}$ must be close to a value of 1840, the ratio of proton and electron rest mass. They find that the optical emission is sufficiently intense to fit an unbroken extension of the radio spectrum, requiring the magnetic field to be relatively low to push an energy-loss break to high frequency. This is something that can be achieved for minimum energy by making $\gamma_{\rm min}$ relatively high. $\gamma_{\rm min}$ is the uncertain factor having greatest influence on the value of $B_{\rm me}$, and $B_{\rm me}$ is roughly proportional to $\gamma_{\rm min}^{-(2\alpha-1)/(\alpha+3)}$ for $\alpha > 0.5$ (e.g. equation 57 of Worrall & Birkinshaw 2006). We see from equations in Section 4.2 that for a fixed frequency of spectral break, τ scales roughly as $\gamma_{\rm min}^{(6\alpha-3)/2(\alpha+3)}$, i.e. $\gamma_{\rm min}^{0.162}$ for $\alpha = 0.7$. That means that for 2152−699 $\gamma_{\rm min}$ could be as low as ∼1 without the lifetime of electrons at the spectral break becoming shorter than the light-crossing time of their emission region.

While the most natural explanation for the X-ray emission from the S hotspot is synchrotron radiation, an interpretation of the N hotspot is more complex, as the X-ray emission is clearly offset from the radio peak (Fig. 8). In the radio peak a synchrotron-emitting electron spectrum that also produces most of the optical emission must cut off at energies less than 7×10^{12} eV (in a minimum-energy magnetic field of ∼13 nT) if it is not to produce detectable X-ray emission at the radio peak (Fig. 19). We have deduced that

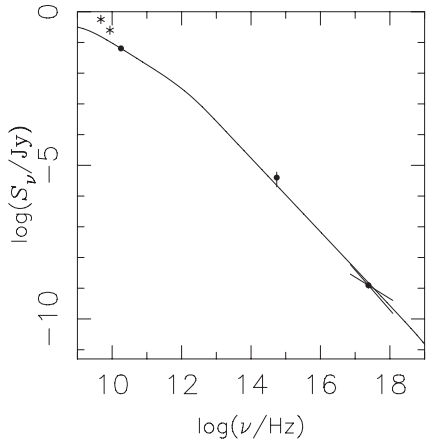

Figure 18. The 18 GHz optical and X-ray measurements of the peak of the S hotspot shown with a power law of $\alpha_r = 0.7$ breaking by $\Delta\alpha = 0.5$ at $\sim 10^{12}$ Hz. The two lowest frequency radio points are from Fosbury et al. (1998) and include emission over a larger region.

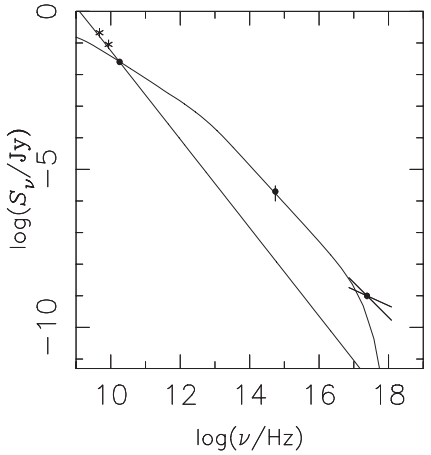

Figure 19. The 18 GHz optical and X-ray measurements of the N hotspot. The flatter curve models the radio peak and optical emission as synchrotron emission that must cut off before the spatially offset X-ray emission. The steeper curve is synchrotron emission in the diffuse part of the hotspot which does not extrapolate to the X-ray emission. The two lowest frequency radio points are from Fosbury et al. (1998).

the S hotspot accelerates electrons to at least 10^{13} eV, and that the N hotspot is unable to accelerate electrons beyond 7×10^{12} eV. Assuming a common acceleration mechanism, it suggests the maximum energy to which it is effective is of order 10^{13} eV rather than much higher, and we are observing regional variations around this value.

As for the S hotspot, the overall N hotspot radio emission, including on larger scales, is too steep in spectrum for a continuation to higher energies to produce the X-rays (Fig. 19). For the X-ray to be synchrotron, its spectrum must extrapolate back to optical and radio frequencies with an index that is flatter than that in the most compact region of the hotspot. This would imply that the electron spectrum is less affected by energy losses than in the more compact component: that is difficult to understand unless particle acceleration is of a different nature and well distributed within the X-ray-emitting region. The hotspot on the jet side of Pictor A has been modelled as flat-spectrum X-ray-synchrotron emission, but there the lack of a spatial offset with the peak of the radio emission allows the X-rays to arise from compact VLBI features, where it is argued that the electron spectrum to high energies is flat because the particles escape from the small acceleration zone before significant energy loss (Tingay et al. 2008). Compact VLBI features (yet to be detected) might be anticipated within the radio peak of 2152−699 but not in the X-ray-emitting region. We therefore conclude that if the X-rays from the N hotspot of 2152−699 are synchrotron radiation, there are implications for the nature and location of particle acceleration that have not previously been modelled in a hotspot.

The X-rays in the N hotspot appear to be associated with the jet as it approaches the peak location of particle acceleration, rather than the hotspot itself. Nothing similar is seen in the south, and it is attractive to consider that the reason is associated with the fact that the N hotspot is on the jet, rather than counterjet, side of the source. The overall hotspot emission cannot be assumed to be strongly affected by relativistic beaming, since the S hotspot, that is associated with the receding jet, is the brighter, even taking only the regions of concentrated emission, and hotspots are generally considered to be relatively static, marking the location where the jet terminates, and advancing only sonically into the external medium. However, the jet plasma could have high relativistic bulk motion as it enters the hotspot, and *Chandra*'s detection of quasar jets, often along their entire length, supports the idea that the flows of FRII jets are not subject to the deceleration common in FRI sources (for a review see Worrall 2009). The X-ray to radio ratio in the X-ray-bright part of the N hotspot is similar to that in knot D, and by analogy an explanation in terms of inverse Compton scattering of CMB radiation would at first seem unlikely (see Section 4.2). However, there is an essential difference. The radio spectrum in the hotspot (except in the peak, offset from the X-ray) is steep spectrum. This is observed within our 18-GHz data, and does not rely on lower frequency measurements of larger beam size. The steep spectrum provides an excess of low-energy particles which are those most effective in scattering the CMB to X-ray energies.

We have modelled the X-ray-bright part of the N hotspot as a cylinder of length 1.7 arcsec and radius 0.78 arcsec (see Fig. 8), with an electron spectrum of $\gamma_{\rm min} = 10$ and the correct slope to produce radio synchrotron radiation of $\alpha_{\rm r} = 1.4$ (Table 1). The minimum-energy magnetic field for a Doppler factor of $\delta = 1$ is found to be $B_{\rm me} \sim 50$ nT, very similar to that in knot D (Section 4.2). Scattering the CMB alone, we can produce the observed X-ray emission if, for example, $\theta = 8^\circ$, and the bulk Lorentz factor and Doppler factor are both ∼7. Smaller angles to the line of sight are also allowed. A value of $\theta = 8^\circ$ is somewhat uncomfortably small for a radio galaxy (Section 4.1). However, as pointed out by Georganopoulos & Kazanas (2003), the bright hotspot synchrotron radiation itself provides a photon field for the approaching jet to scatter and beam in its direction of travel before subsequent abrupt jet deceleration. To get some idea how large an effect this might be, we have estimated the energy density of radio emission from the peak of the N hotspot at the location of the X-ray emission, and used this as an additional scattering field. The availability of the additional photons relaxes the constraint on θ only slightly, but we find $\theta \sim 10^\circ$ ($\delta \sim 5.7$) is now allowed.

An attractive feature of the jet being relatively highly beamed as it enters the hotspot is that $B_{\rm me}$ reduces by a factor of $\delta^{0.77} \sim 4$ from the unbeamed value of ∼50 nT, and now matches our minimum-energy estimate for the peak of the N hotspot (13 nT) where the field is highly ordered (Fig. 7). A slight concern is that the X-ray spectral index would be expected to be steep and match that in the radio. Our X-ray measurement, although poorly constrained, is somewhat flatter (Section 3.4). What is clear is that the N hotspot region, with its offset radio and X-ray emission, has the observational advantage that the X-ray emission is not bright at the hotspot itself, where it can confuse the study of the jet emission. Further sensitive radio and X-ray measurements will allow more detailed modelling and should advance an understanding of jet termination, since the N hotspot region is well suited to sensitive radio and X-ray observation in terms of both angular size and dynamic range.

4.4 The HIC

We calculate the density, pressure and cooling time of the X-ray-emitting gas in the HIC following equations in Worrall & Birkinshaw (2006). The emission measure is defined in terms of the normalization factor returned by XSPEC, N, as

$$10^{14} N = \frac{(1+z)^2 \int n_{\rm e} n_{\rm p}\, {\rm d}V}{4\pi D_L^2}, \tag{1}$$

where $n_{\rm p}$ is the density of hydrogen nuclei, $n_{\rm e}$ is the electron density, V is volume and D_L is luminosity distance. $n_{\rm e} \sim 1.18 n_{\rm p}$ due to the presence of He nuclei (the factor is very weakly dependent on the abundance of heavier elements). This means that for a spherical region of uniform density and angular radius θ, the density and pressure[5] are given by

$$(n_{\rm p}/{\rm m}^{-3}) = 8.5 \times 10^8 (1+z)^2 \sqrt{\frac{(N/{\rm cm}^{-5})}{(D_L/{\rm Mpc})(\theta/{\rm arcsec})^3}}, \tag{2}$$

$$(P/{\rm Pa}) = 3.6 \times 10^{-16} (n_{\rm p}/{\rm m}^{-3})(kT/{\rm keV}). \tag{3}$$

For a monatomic gas the cooling time is then given by

$$(\tau/{\rm Myr}) = \frac{2.9 \times 10^{48} (kT/{\rm keV})(N/{\rm cm}^{-5})(D_L/{\rm Mpc})^2}{(1+z)^2 (n_{\rm p}/{\rm m}^{-3})(L/{\rm erg\,s}^{-1})}, \tag{4}$$

where L is the *bolometric* luminosity of the thermal component. For convenience we express N and L in cgs units since this is how they are returned by XSPEC. The sound speed is

$$(c_{\rm s}/{\rm kpc\,Myr}^{-1}) = 0.54 (kT/{\rm keV})^{0.5}. \tag{5}$$

If we assume that the brightest X-ray emission from the HIC fills a sphere of radius 1.5 arcsec (diameter 1.7 kpc) with uniform density, results of the spectral fit together with equations (2) and

[5] 1 Pa = 10 dyne cm^{-2}.

(3) give a density of $n_p = (7.8 \pm 0.7) \times 10^5\,\mathrm{m}^{-3}$ and pressure of $P = (8 \pm 2) \times 10^{-11}$ Pa. The cooling time (equation 4) is then 15 ± 4 Myr, and represents a maximum lifetime of the gas, unless there is a significant heat source, for which the jet would be a strong contender. Since 2152−699's age may be of order 15 Myr, we cannot differentiate between a situation in which the X-ray emission of the HIC became bright at the onset of the radio source, or become bright more recently.

However, the sound-crossing time presents a more severe constraint. In the absence of confinement by an outer atmosphere, the gas should have suffered adiabatic expansion in roughly its sound-crossing time of 5.8 ± 0.2 Myr (equation 5). While there is a hotter X-ray emitting atmosphere surrounding the HIC gas (Section 3.6), the volume is large and the surface brightness contrast with the HIC gas is much too low for this component to provide the necessary confinement of the HIC. We thus conclude that the HIC X-ray gas is relatively young.

The HIC is only one of the regions adjacent to locations of jet deflection (see Section 4.1). We are not able to determine if X-ray-emitting gas binds the optical feature to the south of knot B, due to the bright readout streak on the deepest X-ray exposures (Fig. 4). There is no evidence of an optical feature where the jet deflects between knots B and C. Momentum transfer from a deflected jet is a natural reason to expect optical filaments, but if the cool gas must be bound by a hot medium, short lifetimes may be the reason that HIC-like features are not more common.

It is interesting that short-lived blobs of X-ray-emitting gas are also observed within a filament lying adjacent to radio emission in the northern middle lobe of Centaurus A (Kraft et al. 2009), where it is suggested that they result from cold gas that has been shock heated by direct interaction with the jet. There too the elemental abundances are low, and it is suggested that this is an artefact of unresolved temperature structure (see also Kim 2012). The same is possible for 2152−699, which would benefit from deeper X-ray observations. It is also possible that the inferred abundances are smaller than the true values if the plasma is photoionized: e.g. Young, Wilson & Shopbell (2001) find low abundances for collisionally ionized models in NGC 1068, while Kinkhabwala et al. (2002) find consistency with solar abundances using photoionization models.

Further understanding of the HIC should result after our approved spatially resolved optical spectroscopy has been carried out. Some of the optical emission may be the result of photoionization from the AGN (Tadhunter et al. 1987; di Serego Alighieri et al. 1988), but the jet deflection in the vicinity of the HIC that is seen in this first detailed mapping supports the idea that direct interaction with the jet has been key to the formation of the HIC (Tadhunter et al. 1988; Tingay et al. 1996; Fosbury et al. 1998). The linear optical structures of the HIC, as seen with *HST*, give the appearance of 'scars', where the jet has passed through and 'ignited' particular gas clouds, where energy is still being dissipated in the form of optical emission lines.

4.5 Lobe inverse Compton emission

If the regions from which lobe X-ray emission is extracted are modelled as prolate ellipsoids, they have volumes of 1.4×10^3 and 4.25×10^3 kpc^3 for the S and N, respectively. The corresponding 4.74 GHz flux densities are 4.44 and 1.98 Jy. The minimum-energy magnetic fields for a fully leptonic plasma whose electron spectrum extends with spectral index of $2\alpha_r + 1 = 2.6$ down to a Lorentz factor of $\gamma_{\min} = 100$ are $B_{\mathrm{me}} \sim 3.1$ and 1.9 nT, with total pressures in the relativistic leptons and field of 2.8×10^{-12} and 1.0×10^{-12} Pa, respectively. The minimum-energy magnetic fields are slightly larger if an energy density in relativistic protons equal to that in leptons is included (3.8 and 2.3 nT, respectively), with corresponding pressures of 4.0×10^{-12} and 1.5×10^{-12} Pa.

To produce the power-law X-ray emission found in our spectral fits from inverse Compton scattering of the CMB, the field values are instead $B = 1.0$ and 0.7 nT, with pressures in relativistic leptons and magnetic field of 1.15×10^{-11} and 3.2×10^{-12} Pa for the S and N lobe, respectively. This level of decrease of the magnetic field strength from minimum energy (assuming no relativistic protons) is commonly estimated in radio galaxies for which the presence of lobe inverse Compton emission is inferred (Croston et al. 2005), and leads to a significant increase in pressure over the minimum-energy value. Since the particles dominate the magnetic field in energy density, the pressure scales directly with the relativistic particle content. Thus if the energy density in relativistic protons equals that in leptons, the corresponding pressures are higher at 2.3×10^{-11} and 6.4×10^{-12} Pa. The lower pressure in the N lobe is consistent with a morphology that suggests less ability to drive a shock into the surrounding gas, consistent with the absence of features bright enough to produce a detectable shock spectral signature.

4.6 The gas structure and radio cavities

The hot gas distribution in 2152−699 is seen sufficiently well in the new *Chandra* observations to reveal some of its complexities. The intensity map (Fig. 15) shows the radio lobes to have evacuated cavities, and the arms of increased X-ray emissivity are suggestive of shock heating by the lobes. The temperature map (Fig. 16) suggests large-scale shifting of gas. This is particularly noticeable to the west of the radio source. The low-frequency (843 GHz) radio map presented by Tadhunter et al. (1988), that represents the location of radio plasma where the particles have aged beyond those in maps presented here, shows the lobes to extend considerably to the west, but cut off sharply in the east. Thus there is reason to believe that gas in our region labelled 'gas' in Figs 5 and 16 has been displaced in the past by radio plasma. As it is cooler than its surroundings, it may now be relatively undisturbed.

The 'gas' region is a 35° pie slice of an annulus (fraction $f = 35/360$) of inner and outer radii $\theta_1 = 24$ arcsec and $\theta_2 = 48$ arcsec, respectively, centred on the nucleus of 2152−699. If the true emission volume is spherical of radius θ_t centred on the nucleus, the line of sight volume, V, is given by

$$V = f D_A^3 \frac{4\pi}{3} \left[\left(\theta_t^2 - \theta_1^2\right)^{3/2} - \left(\theta_t^2 - \theta_2^2\right)^{3/2} \right]. \quad (6)$$

Assuming uniform density between θ_1 and θ_2, the modified version of equation (2) that gives the density in terms of the observables is

$$(n_p/\mathrm{m}^{-3}) = 8.5 \times 10^8 (1+z)^2 \sqrt{\frac{(N/\mathrm{cm}^{-5})}{f(D_L/\mathrm{Mpc})}} \times \left[\left(\theta_t^2 - \theta_1^2\right)^{3/2} - \left(\theta_t^2 - \theta_2^2\right)^{3/2} \right]^{-1/2}, \quad (7)$$

where all values of θ are in units of arcsec. Pressure is given by equation (3). We adopt $\theta_2 = \theta_t$, since the emission is very much fainter beyond θ_2, and in any case the density and pressure cannot be higher than the values given under this assumption. We have also subdivided the annulus in two in radius, and checked that spectral fits are consistent within errors, suggesting no large gradient in temperature or abundance of the gas within the region. Using results in Table 2, the pressure in this region is 1.7×10^{-12} Pa. A similar

argument applied to gas from the 'SE gas' regions finds 1.2×10^{-12} Pa.

The pressure in leptons and magnetic field required to produce the lobe inverse Compton X-ray emission (Section 4.5) is higher than these values for the external gas. This is not unexpected since the lobes have created cavities in the gas. The lobes are therefore expected to drive shocks into the external gas, and be surrounded by cocoons of heated dense gas which should be observable in X-ray observations through increased intensity and temperature. However, the cocoon emission is diluted by foreground and background emission along the line of sight, and in most cavity sources no evidence of such shocked gas is seen (McNamara & Nulsen 2007). 2152−699, however, displays prominent arms of increased emission around the lobes (Fig. 15). We have carried out spectral fitting for the brightest section of the western arm, and the justification for associating gas here (the 'W Arm' region) with a section of such a cocoon lies not only in its increased X-ray intensity but also the evidence that the emission here is hotter (Table 2) than in the regions sampled as being characteristic of unshocked gas.

The pressure ratio between the southern lobe (based on inverse Compton emission for no relativistic protons) and the external gas is 6. This increases to 12 if the energy density in relativistic protons matches that in leptons. Assuming the shocked gas is in pressure balance with the lobe, these ratios are those between shocked and unshocked gas. Using the Rankine–Hugoniot conditions for a strong shock in a monatomic gas (e.g. equations 49–51 of Worrall & Birkinshaw 2006), this pressure ratio relates to the Mach number of the shock via $(5\mathcal{M}^2 - 1)/4$. We thus infer a Mach number in the range 2.2–3, depending on the relativistic proton content. The temperature ratio of shocked and unshocked gas for such a range of Mach number is 2.3–3.7, which could explain the increased temperature seen in the 'W Arm' region once cooler gas along the line of sight to the cocoon is taken into account. The gas contains sufficient structure that it requires complex spatial models to describe fully its distribution. In a forthcoming publication we will address this in more detail.

We have estimated the cavity and 1.4-GHz radio powers, $P_{\rm cav}$ and $P_{1.4}$, respectively, as defined by Cavagnolo et al. (2010). $P_{1.4}$ is $7.7 \times 10^{41}\,{\rm erg\,s^{-1}}$ (Kühr et al. 1981). $P_{\rm cav}$ is raised by a factor of 3 through our use of the dynamical time based on $\mathcal{M} = 3$ and the external sound speed, rather than the buoyant rise time. Despite this, our estimate of the combined cavity power for the two lobes of $P_{\rm cav} \sim 3 \times 10^{43}\,{\rm erg\,s^{-1}}$ falls well below the correlation with radio power of Cavagnolo et al. (2010) ($\sim 2.6 \times 10^{45}\,{\rm erg\,s^{-1}}$) and the earlier correlation of Bîrzan et al. (2008) ($\sim 3.2 \times 10^{44}\,{\rm erg\,s^{-1}}$). However $P_{\rm cav}$ always underestimates the time-averaged jet power, because it ignores work done driving gas and lobe plasma motions and heating shocked gas, and these terms are likely to be particularly important given the strong shock observed in 2152−699. We have estimated the additional energy based on the southern lobe, and doubled the results. We find a kinetic energy of shocked gas, $\frac{1}{2}M_{\rm shock}(\frac{2}{3}v_{\rm shock})^2$ for $\mathcal{M} = 3$, of $\sim 2.4 \times 10^{44}\,{\rm erg\,s^{-1}}$. The mass in shocked gas, $M_{\rm shock}$, uses the region 'W Arm' as a representative cut through a spherical shell of inner and outer radii 19 and 25 arcsec, respectively, whose density is found using equation (7) and the entry in Table 2, and we adopt a shock speed, $v_{\rm shock}$, of three times the sound speed in ambient gas represented by region 'gas'. While the surface brightness peaks in 'W Arm', the shocked region appears broader elsewhere, and we assume the factors balance out in our estimate of $M_{\rm shock}$. A third contribution to the time-averaged jet power ($\sim 7 \times 10^{43}\,{\rm erg\,s^{-1}}$) is from heating the shocked gas from $kT = 0.95$ to 1.33 keV (Table 2). This temperature increase is likely to underestimate that within the shell by a factor of a few, as noted above, and so our total estimated power of expansion $\sim 4 \times 10^{44}\,{\rm erg\,s^{-1}}$ is a conservative estimate. If used instead of cavity power, 2152−699 agrees with the correlation of Cavagnolo et al. (2010), once the large intrinsic scatter of the correlation is taken into account.

Well-defined jet structure means 2152−699 offers a rare possibility of comparing the time-averaged jet power with the instantaneous power in the kpc-scale jet. If we adopt a viewing angle of 10° and beaming with $\delta = 5.7$, which we argued are likely from modelling the N hotspot (Section 4.3) and are consistent with other properties of the jet (Section 4.1), a calculation of the kinetic energy flux (see the appendix of Schwartz et al. 2006) for knot D for leptons only and minimum energy finds $\sim 5 \times 10^{43}\,{\rm erg\,s^{-1}}$. Assuming this is representative of the instantaneous power of the jet, and doubling to take into account the counterjet, we find a shortfall of a factor of $\sim$4 compared with the total time-averaged power above. A modest proton content or small departure from minimum energy in the jet would bring the powers into agreement.

5 SUMMARY

We have reported new results for the jet, hotspots, lobes and environment of 2152−699, a source of great interest not only for the jet–cloud interaction region of its HIC but also as a nearby example of the population of radio galaxies expected to be most typical of radio-mode feedback.

While the radio source is two sided on large scales, with two bright lobes and hotspots, the first high-resolution radio map of the source traces a northern jet more than halfway to its terminal hotspot, but fails convincingly to detect counterjet emission. The source could thus be orientated at relatively small angle θ to the line of sight, although $\theta < 10^\circ$ would be unusual for a radio galaxy with prominent two-sided large-scale structure.

The jet is by no means straight. It extends for $\sim$1.5 kpc as a continuation of the inner component seen in VLBI, and in the direction of the HIC, but then deflects at least twice in a zigzag path before the final deflection that is observed adjacent to the HIC. A new analysis of *HST* data finds optical emission from gas near the jet not only at the HIC but also at the location of the first deflection, although the ionization state of this latter gas is unknown.

Using new *Chandra* data we have concluded that the hot component of gas ($kT \sim 0.3$ keV) associated with the HIC, and almost certainly binding it together, should have dissipated through expansion in $\sim$6 Myr. The HIC is thus a relatively young feature as compared with the likely overall lifetime of the radio source. An unexpected result is the anomalously low metallicity of the HIC X-ray gas – something not seen elsewhere in the larger-scale atmosphere. Deeper X-ray observations are required to test whether this is an artefact of a complex temperature structure, or a physical result that will need considering in the interpretation of forthcoming spatially resolved optical spectroscopy of the HIC. In either case the close association of jet deflection in the new radio data with the location of the HIC supports a strong jet–gas interaction.

We detect optical and X-ray emission from extended lengths of radio jet, as well as the knot close to the HIC. We interpret this emission as synchrotron radiation. An explanation in terms of beamed inverse Compton scattering of the CMB in a minimum-energy jet, as claimed for many quasar jets, would make the angle to line of sight uncomfortably small. Cases of X-ray synchrotron emission over large lengths of an FRII jet are relatively rare, and 2152−699 is one of the best examples. For the knot close to the HIC we deduce an energy-loss time comparable to the light-crossing

time, and so deduce that particle acceleration is continuous within a small region of this knot.

The two hotspots are particularly interesting. Only the southern one emits X-rays in the true 'hotspot' associated with jet termination, where bulk motion is sonic and the radio emission peaks. This region in both hotspots is detected in our ground-based optical observations. We deduce that these emissions are synchrotron, and if there is a common acceleration mechanism in the two hotspots, acceleration of electrons to a maximum energy of $\sim 10^{13}$ eV is suggested.

However, whereas the hotspot X-ray emission on the southern (counterjet) side is concentrated at jet termination, in the north, X-rays are seen only where the jet approaches the hotspot, with the X-ray and radio peaks offset by ∼600 pc. This X-ray emission is difficult to understand unless the jet is oriented at small angle to the line of sight, close to the lower limit expected for radio galaxies ($\theta \sim 10^{\circ}$), and has a bulk relativistic Lorentz factor $\Gamma \sim 5.7$. In that case the X-rays could arise from beamed inverse Compton scattering of CMB and hotspot synchrotron radiation. The interpretation would help to explain the phenomenon being seen in the jet-side hotspot but not the counterjet, and would allow a minimum-energy magnetic field that is similar in the jet and the terminal hotspot, although the interpretation may be in conflict with the X-ray spectral index. Deeper X-ray observations and high-resolution optical measurements with *HST* would help the interpretation of this important situation where we are separating emission from the plasma entering the point of jet termination from the termination point itself.

The large-scale properties of 2152−699 are of particular important in the context of radio-mode feedback. We are rewarded by the new observations displaying multiple features to confirm and measure supersonic expansion of the lobes into the external medium. There are clear depressions in X-ray intensity corresponding to the locations of the radio lobes, indicating that the lobes evacuate cavities in its $kT \sim 1$ keV atmosphere. The X-ray spectra from the regions of the lobes allow separation of components of inverse Compton scattered CMB emission. This has allowed us to estimate the lobe magnetic field strengths and lepton densities, independently of a minimum-energy assumption. As is typical for radio lobes, we find that the magnetic field strengths (∼1.0 and 0.7 nT, in the north and south, respectively) are roughly one-third the minimum-energy values.

The gas distribution is complex, and more complete modelling is the subject of a further paper, but the internal lobe pressure exceeds that in external regions we have modelled by a factor of 6, and greater if relativistic protons add to the lobe's internal energy. This should be driving a shock of Mach number between 2.2 and 3 into the external gas. We find that the kinetic and thermal energy of shocked gas dominates the time-averaged jet power, $\sim 4 \times 10^{44}$ erg s^{-1}, which agrees with our estimate of the instantaneous jet power for only modest proton content or a small departure from minimum energy in the jet if indeed $\theta \sim 10^{\circ}$ and $\Gamma \sim 5.7$. We expected relatively strong shocks like this to be common around expanding radio lobes, but they have proved somewhat elusive, probably largely due to a selection bias towards observing rich atmospheres, where the contrast between shocked and ambient plasma is harder to discern and the ability to separate inverse Compton lobe emission is more difficult. In 2152−699, shocked gas is apparent morphologically as an intensity enhancement, shaping a truncated figure of eight around the lobes. One region is sufficiently bright to allow spectroscopy to a precision sufficient to allow us to conclude that there is a chance less than 1 per cent that it is as cool as ambient gas in regions we have investigated. Deeper X-ray observations will allow us to extend such studies to more regions of the atmosphere, and reach a more complete understanding of the energetics of feedback in this representative source.

ACKNOWLEDGMENTS

We thank staff at Narrabri for help and advice before and during the ATCA observations, and the STFC for travel support. The Australia Telescope is funded by the Commonwealth of Australia for operation as a National Facility managed by CSIRO. We are grateful to the CXC for its support of *Chandra*. We thank the anonymous referee for careful reading of the manuscript and helpful comments.

REFERENCES

Achterberg A., Gallant Y. A., Kirk J. G., Guthmann A. W., 2001, MNRAS, 328, 393
Birkinshaw M., Worrall D. M., Hardcastle M. J., 2002, MNRAS, 335, 142
Bîrzan L., McNamara B. R., Nulsen P. E. J., Carilli C. L., Wise M. W., 2008, ApJ, 686, 859
Böhringer H. et al., 2001, A&A, 365, L181
Bridle A. H., Perley R. A., 1984, ARA&A, 22, 319
Capetti A., Fanti R., Parma P., 1995, A&A, 300, 643
Cavagnolo K. W., McNamara B. R., Nulsen P. E. J., Carilli C. L., Jones C., Bîrzan L., 2010, ApJ, 720, 1066
Celotti A., Ghisellini G., Chiaberge M., 2001, MNRAS, 321, L1
Croston J. H., Hardcastle M. J., Harris D. E., Belsole E., Birkinshaw M., Worrall D. M., 2005, ApJ, 626, 733
David L. P., Jones C., Forman W., Nulsen P., Vritilek J., O'Sullivan E., Giancintucci S., Raychaudhury S., 2009, ApJ, 705, 624
De Vaucouleurs G., De Vaucouleurs A., Corwin H. G., Buta R. J., Paturel G., Fouque P., 1991, Third Reference Catalogue of Bright Galaxies, Ver. 3.9. Springer-Verlag, New York
Dickey J. M., Lockman F. J., 1990, ARA&A, 28, 215
di Serego Alighieri S., Binette L., Courvoisier T. J.-L., Fosbury R. A. E., Tadhunter C. N., 1988, Nat, 334, 591
Fabian A. C. et al., 2011, MNRAS, 418, 2154
Fanaroff B. L., Riley J. M., 1974, MNRAS, 167, 31
Forman W. et al., 2007, ApJ, 665, 1057
Fosbury R. A. E., Morganti R., Wilson W., Ekers R. D., di Serego Alighieri S., Tadhunter C. N., 1998, MNRAS, 296, 701
Georganopoulos M., Kazanas D., 2003, ApJ, 589, L5
Gitti M., Nulsen P. E. J., David L. P., McNamara B. R., Wise M. W., 2011, ApJ, 732, 13
Godfrey L. E. H. et al., 2009, ApJ, 695, 707
Hardcastle M. J., Croston J. H., 2005, MNRAS, 363, 649
Hardcastle M. J., Birkinshaw M., Worrall D. M., 2001, MNRAS, 326, 1499
Hardcastle M. J., Harris D. E., Worrall D. M., Birkinshaw M., 2004, ApJ, 612, 729
Humphrey P. J., Buote D. A., Brighenti F., Gebhardt K., Mathews W. G., 2009, ApJ, 703, 1257
Irwin J. A., Athey A. E., Bregman J. N., 2003, ApJ, 587, 356
Jorstad S. G. et al., 2007, AJ, 134, 799
Kaiser C. R., Best P. N., 2007, MNRAS, 381, 1548
Kataoka J. et al., 2008, ApJ, 685, 839
Kim D.-W., 2012, in Kim, D.-W., Pellegrini, S., eds, Astrophysics and Space Science Library Vol. 378, Hot Interstellar Matter in Elliptical Galaxies. Springer-Verlag, New York, p. 121
Kim D.-W., Fabbiano G., 2004, ApJ, 611, 846
Kinkhabwala A. et al., 2002, ApJ, 575, 732
Kraft R. P., Hardcastle M. J., Worrall D. M., Murray S. S., 2005, ApJ, 622, 149
Kraft R. P. et al., 2009, ApJ, 698, 2036
Kühr H., Witzel A., Pauliny-Toth I. I. K., Nauber U., 1981, A&AS, 45, 367
Ledlow M. J., Owen F. N., 1996, AJ, 112, 9
Ly C., De Young D. S., Bechtold J., 2005, ApJ, 619, 609

McFarland J.-P., Verdoes-Kleijn G., Sikkema G., Helmich E., Boxhoorn D., Valentijn E., 2011, Exp. Astron., 129
McNamara B. R., Nulsen P. E. J., 2007, ARA&A, 45, 117
Marshall H. L. et al., 2010, ApJ, 714, 213
Norris R. P. et al., 1990, Proc. Astron. Soc. Australia, 8, 252
Perlman E. S., Georganopoulos M., May E. M., Kazanas D., 2010, ApJ, 708, 1
Saikia D. J., 1999, MNRAS, 302, L60
Schilizzi R. T., McAdam W. B., 1975, Mem. R. Astron. Soc., 79, 1
Schwartz D. A. et al., 2006, ApJ, 640, 592
Stawarz Ł., Sikora M., Ostrowski M., 2003, ApJ, 597, 186
Tadhunter C. N., Fosbury R. A. E., Binette L., Danziger I. J., Robinson A., 1987, Nat, 325, 504
Tadhunter C. N., Fosbury R. A. E., di Serego Alighieri S., Bland J., Danziger I. J., Goss W. M., McAdam W. B., Snijders M. A. J., 1988, MNRAS, 235, 403
Tingay S. J. et al., 1996, AJ, 111, 718
Tingay S. J., Lenc E., Brunetti G., Bondi M., 2008, AJ, 136, 2473
Unger S. W., Lewis J. R., Pedlar A., Axon D. J., 1992, MNRAS, 258, 371
Vandame B., 2004, PhD thesis, Université de Nice
Wilson A. S., Young A. J., Shopbell P. L., 2001, ApJ, 547, 740
Wilson W. E. et al., 2011, MNRAS, 416, 832
Worrall D. M., 2009, A&AR, 17, 1
Worrall D. M., Birkinshaw M., 2005, MNRAS, 360, 926
Worrall D. M., Birkinshaw M., 2006, in Alloin D., Johnson R., Lira P., eds, Lecture Notes in Physics Vol. 693. Springer-Verlag, Berlin, p. 39
Worrall D. M., Birkinshaw M., Hardcastle M. J., 2001, MNRAS, 326, L7
Worrall D. M., Birkinshaw M., O'Sullivan E., Zezas A., Wolter A., Trinchieri G., Fabbiano G., 2010, MNRAS, 408, 701
Young A. J., Wilson A. S., Shopbell P. L., 2001, ApJ, 556, 6
Young A. J., Wilson A. S., Tingay S. J., Heinz S., 2005, ApJ, 622, 830

This paper has been typeset from a TEX/LATEX file prepared by the author.